A tunable wavelength pump apparatus with arbitrary repetition rate for time- and angle-resolved photoemission spectroscopy

A Thesis presented

by

Michael J. Wahl

to

The Graduate School

in Partial Fulfillment of the

Requirements

for the Degree of

Master of Science

in

Physics

(Instrumentation)

Stony Brook University

May 2024

Stony Brook University

The Graduate School

Michael J. Wahl

We, the thesis committee for the above candidate for the

Master of Science degree, hereby recommend

acceptance of this thesis

Thomas K. Allison - Thesis Advisor
Associate Professor, Department of Physics and Astronomy

Abhay Deshpande - Committee Member
Distinguished Professor, Department of Physics and Astronomy

Peter Stephens - Committee Member
Distinguished Professor Emeritus, Department of Physics and Astronomy

This thesis is accepted by the Graduate School

Celia Marshik
Dean of the Graduate School

Abstract of the Thesis

A tunable wavelength pump apparatus with arbitrary repetition rate for time- and angle-resolved photoemission spectroscopy

by

Michael J. Wahl

Master of Science

in

Physics

(Instrumentation)

Stony Brook University

2024

Time- and angle-resolved photoemission spectroscopy (TR-ARPES) experiments strongly benefit from varying the wavelength of the pump laser, which permits direct excitation of electronic states over a range of energies. The long acquisition times of TR-ARPES can be assuaged by using pulsed lasers of MHz-scale repetition rates, but some sample relaxation effects can take longer than the nominal pulse period. Thus the most flexible pump sources would have both a tunable wavelength and repetition rate. In this thesis, I first present an arbitrary repetition rate laser based on a nonlinear Er:doped fiber amplifier capable of producing 100 kW peak power pulses. Successive broadening in highly nonlinear fibers generates a NIR supercontiuum. Second, I describe an amplification system based on optical parametric amplification that is capable of producing up to 8 nJ pulses with 660-800 nm wavelength tunability while maintaining arbitrary (0-60 MHz) repetition rate operation. In parallel with our existing, fully synchronized XUV source, this next generation light source will enable the study of new interactions and materials with TR-ARPES.

Contents

List of Figures

List of Tables

Acknowledgements

I'd like to express my thanks to the many mentors that have guided me through this journey. I am grateful to Kevin Werner, Anthony Catanese, and Yannick Morel at BAE Systems for showing me the ropes of measuring femtosecond lasers. Thank you to Tom Weinacht, who taught me much of what I know about using femtosecond lasers to do good science, as well as his students Michael and Julia, with whom I first cut my teeth on hands-on laser development. I am indebted to Tom Allison, whose enthusiam as an advisor motivated me to accomplish as much as I have with this project. His students Yuanchi and Myles taught me their optical fiber wizardry, which is also much appreciated. Special thanks goes to Hal Metcalf, who gave me my first introduction to the world of formal academic research, and without whom I would not have continued to graduate school.

Chapter 1

Introduction

1.1 Time- and Angle-Resolved Photoemission Spectroscopy

Photoemission spectroscopy (PES) is a common and effective method of probing materials which relies on the photoelectric effect [1, 2]. Famously explained by Einstein in 1905, photoemission experiments use lasers, synchrotrons, and other high photon energy sources to overcome the work function of solids and eject electrons from their surfaces. These electrons are emitted in a broad spectrum of energies, and these can be analyzed to reveal the energy levels of the sample.

Fully characterizing the electronic structures of solid-state samples is challenging, as their band structures have explicit momentum dispersion. This necessitates a momentum measurement in conjunction with an energy measurement. Angle-resolved PES (ARPES) can deduce the electron's initial momentum vector within the crystal by measuring its final momentum vector after photoemission. Simultaneous energy and momentum measurements can be performed with advanced time-of-flight momentum microscope (ToF k-mic) detectors such as in Figure 1.1 [3–5].

Conventional ARPES can only probe occupied electronic states, namely those below the Fermi level. Thus, if one wishes to map the electronic structures of states above the valence band, one needs another light source capable of exciting these states first, such as the scheme in Figure 1.1. The necessity of a second source also introduces the ability to vary the relative time delay and resolve the temporal dynamics (TR-ARPES).

TR-ARPES is used to study a variety of fundamental physics. In past experiments, our lab has studied the behavior of electrons in monolayer graphene near the Dirac points [6]. Figure 1.2 depicts TR-ARPES data of the six Dirac points in momentum space. Variation of the pump polarization cause a clear shift in the distribution of excited electrons which we attribute to graphene's lattice pseudospin polarization.

A recent topic of interest is the formation of excitons in transition metal

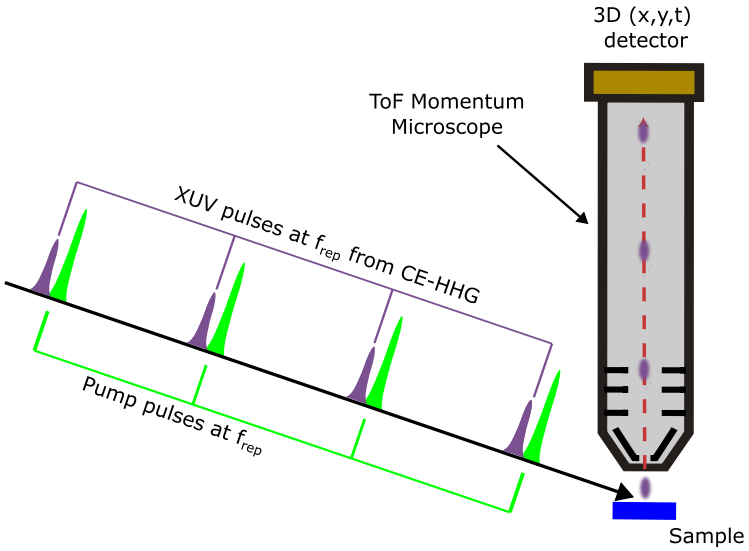

Figure 1.1: An ultrashort pump laser pulse (typically visible or infrared) is absorbed by a solid surface, exciting electrons into the conduction band. After an adjustable time delay, an ultrashort probe pulse (here, in the extreme UV), ejects an electron from the surface. The momenta and energy of the electrons are detected in a ToF k-mic.

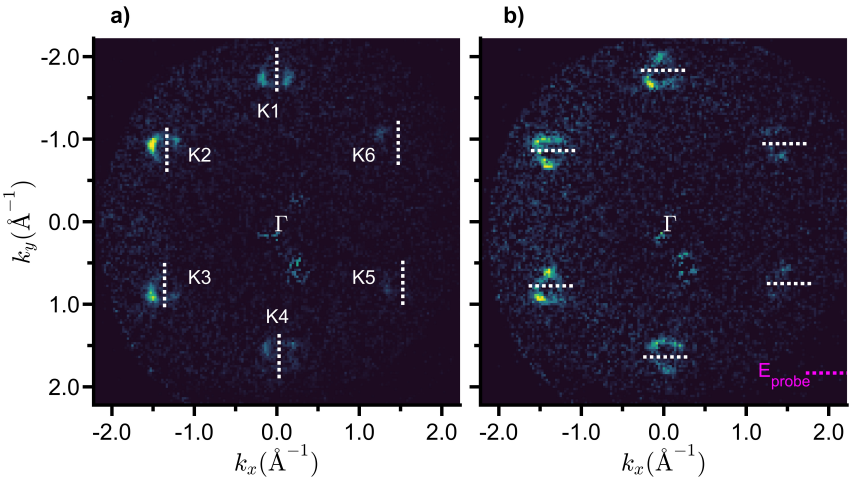

Figure 1.2: TR-ARPES data highlighting the Dirac (K) points of graphene in momentum space. The distribution of excited electrons changes between p-polarized (left) and s-polarized (right) 517 nm pump light, which we attribute to lattice pseudospin polarization.

dichalcogenides (TMDs), especially in heterostructures formed from stacking multiple TMD monolayers [7–9]. We have already demonstrated measurements of excitons in one of these TMDs, monolayer WS_2 [10], but limitations of the pump apparatus prevented us from performing experiments of WSe_2, MoS_2, $MoSe_2$, and corresponding heterostructures.

The WSe_2, $MoSe_2$, and MoS_2 A-exciton transitions are around 2.0 eV, 1.6 eV, and 1.9 eV, respectively, each with bandgaps of less than 2.4 eV [11]. If were were to study these materials with the 2.4 eV pump used in the WS_2 experiments, we would instead see a conduction band signal. Studying these material requires a pump of tunable wavelength.

Additionally, the study of interlayer excitons (ILXs) in TMD heterostructures uniquely benefits from adjustable pump photon energies. Heterostructures are composed of two different TMD monolayers, which allows for selective excitation of one layer's exciton or the other [8]. These monolayer excitons can then relax into ILXs, where the electron and hole components are separated across TMD monolayers [12]. The ability to selectively control the formation pathway of the ILX via tunable photon energy is invaluable.

1.2 Designing a Laser for TR-ARPES

1.2.1 Experimental Considerations

There are several important considerations when designing a laser system for TR-ARPES:

Photon Energies The photon energy of the probe must exceed the work function of the material, and should ideally greatly exceed the work function to access high-k electrons. TMD excitons in particular exhibit their characteristic behavior at the edge of the Brillouin zone, which is only accessible with XUV photons.

The energy of pump photons is also important. Ideally, pump photons excite the state of interest, and should not exceed it by too much lest higher states may be errantly populated. This is especially true for states with transitions near the bandgap like excitons, which would be washed out by conduction band signal.

Pulse Duration Time-resolved data resolution can be limited by the pulse duration of the pump and/or probe. Pulse durations should be shorter than the desired timing resolution.

Pulse Energy/Repetition Rate The excited state signal of TR-ARPES is minuscule compared to the ground state, as only a fraction of atoms illuminated by the pump are actually excited. To improve the data rate, more excited electrons must be sent to the detector by increasing four factors [13]:

$$\begin{aligned}\text{Data Rate} \propto (\text{repetition rate}) \times (e^{-}\text{collection efficiency}) \\ \times (\text{pump fluence}) \times (\text{probe fluence})\end{aligned} \tag{1.1}$$

Electron detection efficiency is already excellent when using a ToF k-mic, and the probe fluence is limited by the space charge effect [14]. High pump fluences can increase the probability of excitation, but directly studying the dynamics of quasi-particles (e.g. excitons) limits the pump fluence to the μJ/cm^2 regime.

Instead, gains are made by increasing the repetition rate of the laser. However, some electronic relaxations, such as interlayer excitons in TMD-TMD [15] and TMD-pentacene [16] heterostructures, take longer than the pulse-to-pulse period to return fully to the ground state. Re-pumping a state before it is completely relaxed can result in a build-up effect which complicates the measurement. Thus, the repetition rate is limited by the time scale of the dynamics in question.

In order to keep data acquisition times reasonable, optimizing the pump laser is essential. Ideally, one would be able to independently control the wavelength, pulse energy, and repetition rate to collect data from a variety of samples as quickly as possible.

1.2.2 The Design Before Tunable Pump

The straightforward solution to synchronizing the pump and probe is to derive the both from the same oscillator, but the drastically different photon energies of the respective beams require an elaborate nonlinear frequency conversion process. To obtain high photon energy probe pulses on a tabletop scale, one can perform high harmonic generation (HHG) in a gas [17].

HHG is understood with the three-step model, where intense laser fields first create tunneling ionization, then energetically recombine electrons with their host atoms [18]. The pulse energies needed to achieve HHG are typically $\sim$100 μJ in the IR. HHG with in the visible is possible with $\sim$10 μJ pulses, but this geometry produces fewer, less energetic harmonics which are more widely spaced in frequency [19]. This is not ideal for large, continuous scans of probe photon energy.

With kHz lasers, HHG with a NIR laser is possible at average powers of $<$ 10 W in a single pass. In order to optimize TR-ARPES data rates, repetition rates around 100 MHz are preferable, but this requires multi-kW average powers. Although impractical with a single pass system, these powers are possible by utilizing a high-finesse enhancement cavity. However, gas ionization presents limitations on the finesse of such HHG cavities, so these intracavity powers still require $\sim$100 W driving lasers [20].

All of these considerations led to the development of the high-power Yb laser system detailed in Li et. al. [21]. This system used a home-built Yb:fiber

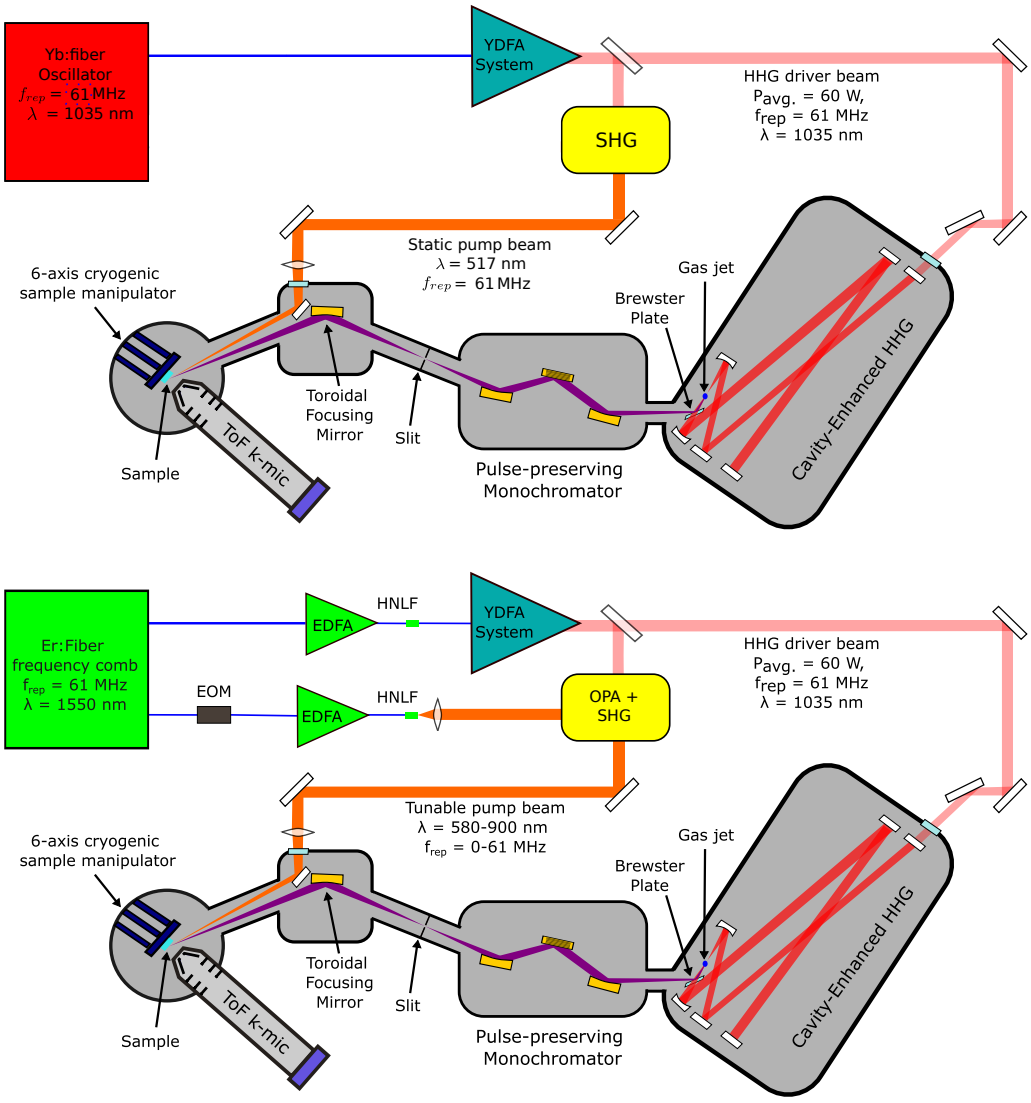

Figure 1.3: (top) TR-ARPES laser system prior to 2023. (bottom) Laser system after swapping the oscillator to a commercial Er:fiber device and upgrading the pump arm to a tunable wavelength and arbitrary repetition rate.

oscillator centered at 1035 nm to drive a two stage (later upgraded to three stage) chirped-pulse Yb:fiber amplifier. With this oscillator, the system produced ∼155 fs pulses of 1μJ at 88 MHz repetition rate. This laser coupled into an enhancement cavity which produced XUV probe light through HHG [22,23]. The plethora of 1035 nm light could simultaneously drive a static 517 nm pump via second harmonic generation.

The major roadblock of this laser system was the static pump. This limited the types of samples we could study to those which have an electronic excitation around 2.4 eV, such as the aforementioned graphene and monolayer WS_2 [6, 10].

1.2.3 After Tunable Pump

The ability to simultaneously control the wavelength, repetition rate, and, pulse energy is invaluable for TR-ARPES as it allows a single apparatus to study a wide variety of materials. In particular, a tunable pump photon energy of 1.6-2 eV would unlock the study of additional TMD excitons.

The home-built Yb:fiber oscillator has been replaced by a stable, low-noise commercial Er:fiber oscillator with a slightly lower repetition rate of 60 MHz. To seed the Yb:fiber amplifier and HHG cavity (which remain unchanged), we use a nonlinear Er:fiber amplifier (EDFA) to shift the wavelength of the 1550 nm Er:fiber oscillator light to 1035 nm, as seen in Figure 1.3.

The new pump arm also implements a nonlinear EDFA along with a polarization modulation scheme used to achieve arbitrary repetition rate. Afterwards, an optical parametric amplifier (OPA) amplifies a narrow, tunable band of the NIR nonlinear EDFA spectrum (1320-1600 nm), and successive second harmonic generation creates a tunable wavelength pulse (660-800 nm, 1.55-1.88 eV) . The following chapters detail the specifics of creating such a system.

1.3 Overview

Chapter 2 outlines the relevant theory of nonlinear optics used in this thesis. Chapter 3 describes the arbitrary repetition rate, 100 kW peak power Er:fiber laser as well as the generation of new spectral components in the NIR. This is followed by Chapter 4, which delineates the amplification/frequency conversion scheme used to create 8 nJ, 660-800 nm pulses from the Er:fiber laser. Chapter 5 concludes the thesis with a discussion of future improvements to the apparatus as well as the broader scientific and engineering impact of this repetition rate tuning scheme.

Chapter 2

An Introduction to Nonlinear Optics

The following chapter provides a basic understanding of the mathematical descriptions and terminology used in Chapters 3 and 4. For more detail, consult the excellent, comprehensive textbooks of Boyd [24] and Agrawal [25].

2.1 The Nonlinear Susceptibility

Light's strongest interaction with non-relativistic matter is through the electric field, and can be described in bulk materials by the dipole moment per unit volume, or polarization, P. It can be described by a power series expansion in vector form:

$$\begin{aligned}\tilde{\mathbf{P}}(t) &= \epsilon_0 \left(\chi^{(1)} \cdot \tilde{\mathbf{E}} + \chi^{(2)} : \tilde{\mathbf{E}}\tilde{\mathbf{E}} + \chi^{(3)} \vdots \tilde{\mathbf{E}}\tilde{\mathbf{E}}\tilde{\mathbf{E}} + ...\right) \\ &= \tilde{\mathbf{P}}^{(1)}(t) + \tilde{\mathbf{P}}^{(2)}(t) + \tilde{\mathbf{P}}^{(3)}(t) + ... \ ,\end{aligned} \tag{2.1}$$

where $\tilde{\mathbf{P}}(t)$ is the rapidly time-varying polarization, and $\tilde{\mathbf{E}}$ is the driving electric field from the laser. Introduced here are the susceptibility tensors $\chi^{(n)}$, with the second- and third-order nonlinear susceptibilites ($\chi^{(2)}$ and $\chi^{(3)}$) producing second- and third-order nonlinear polarizations ($\tilde{\mathbf{P}}^{(2)}(t)$ and $\tilde{\mathbf{P}}^{(3)}(t)$). The expansion can be carried out to even higher orders, but most practical applications consider only $\chi^{(2)}$ and $\chi^{(3)}$ effects.

In non-isotropic media such as optical crystals, the tensorial nature of $\chi^(n)$ is an important factor. Lasers which take advantage of nonlinear optics in crystals often attempt to use the strongest elements of χ with particular orientations and polarizations of light. For geometries with fixed propagation directions and polarizations, it is possible to relate the scalar value of the nonlinear polarization to the driving electric fields through a single constant d_{eff}. This constant is derived from the terms of the susceptibility tensor and the geometry [24].

This treatment of the nonlinear polarization assumes an instantaneous response of the electrons to the surrounding electric fields, and is adequate to explain self- and cross-phase modulation, three- and four-wave mixing, and most other effects discussed in this chapter. An approach analyzing the delayed nonlinear response is necessary to explain Raman scattering.

2.2 The Nonlinear Wave Equation

In linear optics, Maxwell's equation produce the wave equation for light in a medium:

$$\nabla^2\tilde{\mathbf{E}} - \frac{n^2}{c^2}\frac{\partial^2\tilde{\mathbf{E}}}{\partial t^2} = 0. \tag{2.2}$$

The linear polarization response creates a screening effect which reduces the phase velocity of the light, called the refractive index (n). In nonlinear optics, the nonlinear polarization terms (collectively $\tilde{\mathbf{P}}^{NL}$) produce:

$$\nabla^2\tilde{\mathbf{E}} - \frac{n^2}{c^2}\frac{\partial^2\tilde{\mathbf{E}}}{\partial t^2} = \frac{\partial^2\tilde{\mathbf{P}}^{NL}}{\partial t^2}. \tag{2.3}$$

The nonlinear polarization becomes a driving term to the wave equation, and thus produces new light frequencies as the anharmonic electric dipoles of the surrounding atoms emit coherent radiation. By combining the the nonlinear polarization and the nonlinear wave equation, one can mathematically describe many types of nonlinear optical effects. These include three- and four-wave mixing, optical rectification, the optical Kerr effect, and many others.

2.3 Three Wave Mixing

First, we consider interactions of order $\chi^{(2)}$. For centrosymmetric materials (i.e. those that exhibit inversion symmetry) such as glass, $\chi^{(2)}$ vanishes in the bulk. Many crystals such as lithium niobate (LN), β-barium borate (BBO), and potassium titanyl phosphate (KTP) have complex crystal structures which break this symmetry and have non-zero $\chi^{(2)}$.

In our research, laser beams are typically tightly focused, broadband, pulsed light. Adopting for now the engineering sign convention of the traveling wave, we write the rapidly varying scalar electric field:

$$\tilde{E}(z,t) = \frac{1}{2}A(z,t)e^{i(\omega t - kz)} + \text{c.c.}, \tag{2.4}$$

where ω is the "carrier" frequency of the oscillation, and $A(z,t)$ is the slowly varying complex envelope of the pulse such that:

$$\left|\frac{\partial^2 A}{\partial z^2}\right| \ll 2k\left|\frac{\partial A}{\partial z}\right|. \tag{2.5}$$

If two such beams are combined in a crystal with $\chi^{(2)}$ nonlinearity, Eqs. 2.1 and 2.3 construct a set of three coupled differential equations. The interaction of the beams along the direction of propagation is approximately described by [26]:

$$\begin{aligned}
\frac{\partial A_1}{\partial z} + \frac{1}{2i}\beta_2(\omega_1)\frac{\partial^2 A_1}{\partial \tau^2} + \delta_{13}\frac{\partial A_1}{\partial \tau} &= -i\frac{d_{eff}\omega_1}{n_1 c}A_2^* A_3 e^{-i\Delta k z} \\
\frac{\partial A_2}{\partial z} + \frac{1}{2i}\beta_2(\omega_2)\frac{\partial^2 A_2}{\partial \tau^2} + \delta_{23}\frac{\partial A_2}{\partial \tau} &= -i\frac{d_{eff}\omega_2}{n_2 c}A_1^* A_3 e^{-i\Delta k z} \\
\frac{\partial A_3}{\partial z} + \frac{1}{2i}\beta_2(\omega_3)\frac{\partial^2 A_3}{\partial \tau^2} &= -i\frac{d_{eff}\omega_3}{n_3 c}A_1 A_2 e^{i\Delta k z}.
\end{aligned} \tag{2.6}$$

n_i are the refractive indexes at frequencies ω_i for $\omega_3 = \omega_1 + \omega_2$. $\beta_2(\omega_i)$ are the group velocity dispersions at ω_i such that for the group velocity $v_g(\omega)$,

$$\beta_2(\omega_i) = \frac{\partial}{\partial \omega}\left(\frac{1}{v_g(\omega)}\right)_{\omega=\omega_i} = \left(\frac{\partial^2 k}{\partial \omega^2}\right)_{\omega=\omega_i} \tag{2.7}$$

Group velocity dispersion is also often written as "GVD", but fiber optics prefers the β_2 convention which we also adopt. $\delta_{ij} = 1/v_g(\omega_i) - 1/v_g(\omega_j)$ is the group velocity mismatch (GVM). τ is defined by the frame of reference corresponding to the group velocity of ω_3 (i.e. v_{g3}) such that $\tau = t - z/v_{g3}$. Finally,

$$\begin{aligned}
\Delta k &= k(\omega_3) - k(\omega_2) - k(\omega_1) \\
&= k_3 - k_2 - k_1.
\end{aligned} \tag{2.8}$$

Eq. 2.8 is referred to as the phase matching condition or the wavevector mismatch, the intricacies of which are explained in Section 2.4. In $\chi^{(3)}$ materials, a similar four-wave mixing (FWM) process occurs. The derivation and behavior are nearly identical to three-wave mixing [24].

2.3.1 Parametric Amplification

Optical parametric amplification, or OPA, shares its acronym with the device used to produce it, the optical parametric amplifi*er*. OPA relies on the equations of three-wave mixing (Eq. 2.6), where a strong "pump" beam at ω_3 and a weak "signal" beam at ω_1 are incident on a $\chi^{(2)}$ crystal. Each pump photon is converted into one signal and one "idler" photon at the difference frequency $\omega_2 = \omega_3 - \omega_1$ (see Fig. 2.1).

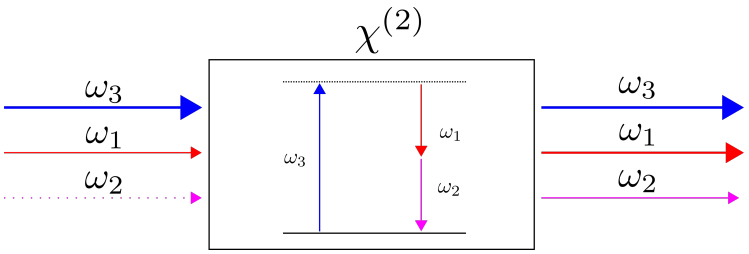

Figure 2.1: Intense pump light of frequency ω_3 enters a crystal with $\chi^{(2)}$ nonlinearity along with a weak signal at ω_1. A single pump photon coherently produces a pair of photons, one at the signal frequency ω_1, and a second at the difference frequency (or idler) ω_2. Typically, no input field is applied at ω_2.

For OPA systems that primarily care about amplification of the signal (such as our own), the idler is discarded. Some systems use OPA explicitly to generate idler light. Such techniques are useful for creating coherent, high power MIR sources which can be challenging to produce directly with lasers [27].

2.3.2 Second Harmonic Generation

A degenerate case of three wave mixing, second harmonic generation (SHG) generates light at twice the frequency of the incoming laser field. The degeneracy means that A_1 and A_2 in Eq. 2.6 both refer to the fundamental laser frequency, indicating that as second harmonic (A_3) field is produced, the fundamental pump field is depleted at twice the rate. This lends itself to an analogous interpretation of SHG illustrated in Figure 2.2, where a pair of pump photons at frequency ω_1 convert directly into a single photon at the second harmonic.

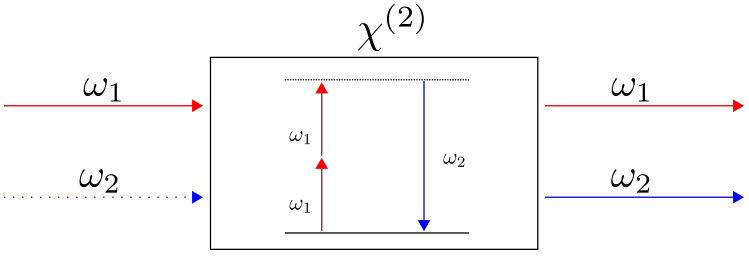

Figure 2.2: Pump photons of frequency ω_1 enter a crystal with $\chi^{(2)}$ nonlinearity. For each two pump photons, a single photon at the second harmonic (ω_2) is coherently produced. Typically, no input field is applied at ω_2.

2.4 Phase Matching

A primary consideration when choosing a nonlinear crystal is the phase matching condition:

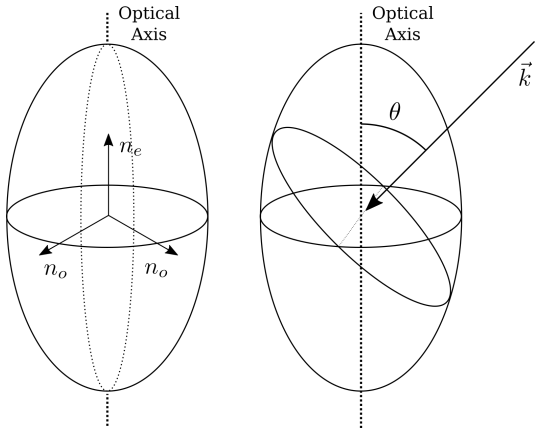

Figure 2.3: The refractive indicatrix for a positive uniaxial crystal is an ellipsoid with two unique principle axes (i.e. a football). The refractive indexes of ordinary and extraordinary polarized light is found by considering the orthogonal cross-section to $\vec{k}$. For uniaxial crystals, this is uniquely determined by the angle θ between the optical axis and the k-vector of incoming radiation.

$$\Delta k = k_3 - k_2 - k_1 = 0. \tag{2.9}$$

If the phase matching condition is not satisfied, the coherent emissions of the electric dipoles interfere destructively, and produce little to no macroscopic effect.

In vacuum, the phase matching condition is trivial, but in media, the refractive index varies with the optical frequency:

$$\Delta k = \frac{\omega_3 n(\omega_3)}{c} - \frac{\omega_2 n_(\omega_2)}{c} - \frac{\omega_1 n(\omega_1)}{c}. \tag{2.10}$$

This limitation can be overcome in a number of ways, namely through birefringent phase matching (both critical and non-critical) or quasi-phase matching.

2.4.1 Birefringent Phase Matching

Some crystal structures allow for birefringence, that is, the variation of the refractive index with the direction of polarization. For uniaxial crystals such as LN and BBO, n is characterized along the two unique principal axes of the crystal, the ordinary index (n_o, 2 axes) and the extraordinary index (n_e, 1 axis). Positive uniaxial crystals, such as in the example refractive indicatrix in Fig. 2.3, have a larger n_e than n_o, with negative uniaxial crystals like LN and BBO having the opposite relationship. The optical axis, or the propagation direction in which light experiences no birefringence, happens to align with the extraordinary axis. True to their name, uniaxial crystals only have one such axis.

When light propagates at some angle θ from the optical axis, light polarized orthogonal to the optical axis experiences the refractive index n_o, and is said to have ordinary polarization. Light of the opposite polarization feels a refractive index between n_o and n_e that is dependent on θ [26]:

$$\frac{1}{n_e(\theta)^2} = \frac{\cos^2(\theta)}{n_o^2} + \frac{\sin^2(\theta)}{n_e^2}, \tag{2.11}$$

and is said (somewhat confusingly) to have extraordinary polarization. In certain crystals with strong enough birefringence, it is possible to satisfy phase matching by cutting the crystal at angle θ. The strength of the birefringence is greatly dependent on the wavelengths at play, and generally decreases with the wavelength.

The birefringence can be further tuned by tilting the crystal itself (critical phase matching) or by changing its temperature (non-critical phase matching). In geometries such as Type I phase matching ($o + o = e$ or $e + e = o$), newly produced light is emitted at an orthogonal axis to the input beam(s). By contrast, Type II phase matching ($o + e = o$ or $e + o = e$) uses input beams at orthogonal polarizations.

An unfortunate downside of birefringent phase matching is the heavy restrictions it imposes on the interaction. There are typically only one or two configurations of polarization and angle/temperature that correctly phase match (if any), which inhibits flexibility in the beam geometry and often uses a d_{eff} much less than the maximum possible for the crystal. Additionally, extraordinary polarized light does not have a Poynting vector $\mathbf{S}$ parallel to its k-vector. This results in spatial walkoff, where the power of the extraordinary beam wanders away from the ordinary beams and limits interaction strengths and/or crystal lengths.

2.4.2 Quasi-Phase Matching

As opposed to birefringent phase matching, quasi-phase matching (QPM) typically utilizes three parallel light polarizations. It accomplishes this with a special manufacturing process called periodic polling, which periodically inverts the crystal structure (Fig. 2.4).

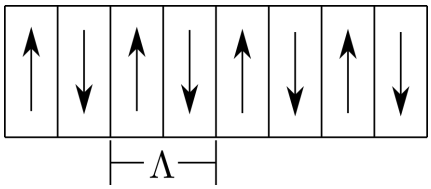

Figure 2.4: To implement QPM, the crystal axis is inverted and reverted at a polling period Λ.

Periodically inverting the crystal structure inverts the sign of d_{eff} and effectively modifies the phase matching condition, which becomes:

$$\Delta k = k_3 - k_2 - k_1 - \frac{2\pi}{\Lambda}, \tag{2.12}$$

where Λ is the polling period. This allows the condition to be satisfied solely by changing Λ.

This additional freedom allows geometries which take full advantage of the largest possible d_{eff}. However, this is only a benefit if the increase in d_{eff} is greater than the reduction of $2/\pi$ caused by the periodic polling. Often, the largest d_{eff} is for beams of parallel polarizations which cannot use birefringent phase matching. QPM also allows the use of crystals with low birefringence or none at all. Periodic polling is only possible with ferroelectic crystals, and the difficulty of the manufacturing process dramatically increases cost and complexity.

Higher Order QPM

The periodic polling process also introduces higher order effects. When the polling period is an even multiple of the first order QPM period Λ, complete destructive interference occurs, as the amplitude is in-phase as much as it is out of phase. When the polling is an odd multiple of the first order, partial QPM is maintained. For example, at 3Λ, the first 2Λ of the polling period produces no net effect, with only the last Λ length providing the phase matching necessary to make macroscopic contributions to the interaction. These effects are often disregarded due to the inefficient nature of wasting crystal length, but parasitic processes which properly phase match at higher orders can steal power away from the intended signal and/or idler.

2.4.3 Phase Matching Ultrashort Pulses

Ultrashort pulses are supported by broad bandwidths, but these polychromatic beams pose difficult questions when it comes to phase matching. A single crystal angle or polling period may solve the phase matching condition perfectly for monochromatic light, but pulsed light has several key limitations.

The first is caused by GVM (δ_{ij}). The difference in group velocities causes the pulses to temporally separate as they propagate through the crystal. In the absence of gain, we can introduce the pulse-splitting length between the signal/idler (ω_1, ω_2) and pump (ω_3) [26]:

$$l_{j3} = |\tau/\delta_{j3}|\,. \tag{2.13}$$

While certain geometries and crystals enable additional gain for lengths exceeding l_{j3}, it nonetheless serves as an important metric beyond which one must consider temporal walkoff effects.

The second issue is cause by GVD. GVD causes the phase of light $+\delta^{(+)}\omega_1$ and $-\delta^{(-)}\omega_1$ away from the central signal frequency ω_1 to slip away from constructive interference, but the amplitude of the signal still adds constructively

when for a crystal of length L:

$$\begin{aligned} -\pi < \Delta k L < \pi \\ (k(\omega_3) - k(\omega_1 + \delta^{(+)}\omega_1) - k(\omega_2 - \delta^{(+)}\omega_1))L < \pi \\ (k(\omega_3) - k(\omega_1 - \delta^{(-)}\omega_1) - k(\omega_2 + \delta^{(-)}\omega_1))L > -\pi \\ . \end{aligned} \tag{2.14}$$

The acceptance bandwidth is then defined as $|\delta^{(+)}\omega_1 + \delta^{(-)}\omega_1|$. Note that the above definition is 13% greater than the FWHM of the mixing efficiency [28]. The mixing bandwidth can be approximated by the GVM and GVD of the interacting pulses, but can also be found more precisely by numerically calculating the dispersion of Δk from the dispersion of $k(\omega)$ [26]. Typically given in THz·cm, this introduces an important tradeoff between the amount of bandwidth participating in the nonlinear interaction and the gain of said interaction (i.e. the length).

2.5 The Intensity-Dependent Refractive Index

Since fused silica glass is a centrosymmetric material, $\chi^{(2)} \equiv 0$. All optical fibers we will consider have this property, thus their nonlinearities can be described as $\chi^{(3)}$ interactions. $\chi^{(3)}$ is responsible for a litany of effects, such as four-wave mixing, self-focusing, and self-phase modulation. The latter two can be understood in the context of how $\chi^{(3)}$ induces an intensity-dependent refractive index.

We begin by studying a linearly polarized plane wave which produces a scalar polarization:

$$\tilde{P}(t) = \epsilon_0 \left(\chi^{(1)} \tilde{E}(t) + \chi^{(3)} \tilde{E}(t) |\tilde{E}(t)|^2 \right). \tag{2.15}$$

The linear polarization allows us to suppress the tensor nature of $\chi^{(n)}$. The rapidly time varying electric field $\tilde{E}(t)$ uses the same convention as Eq. 2.4, but can be expressed without the z dependence in the Fourier domain:

$$\tilde{E}(t) = \frac{1}{2} A(\omega) e^{i\omega t} + \text{c.c.} \ . \tag{2.16}$$

$A(\omega)$ is the slowly varying amplitude of the plane wave at frequency ω. The refractive index can generally be written as:

$$n = \sqrt{1 + \chi_{eff}}, \tag{2.17}$$

where:

$$\tilde{P}(t) = \epsilon_0 \chi_{eff} \tilde{E}(t). \tag{2.18}$$

When considering only the linear response ($\chi^{(1)}$), this gives the linear refractive index n_0. Including the $\chi^{(3)}$ contribution:

$$\tilde{P}(t) = \epsilon_0 \Bigg(\frac{1}{2}\chi^{(1)}(A(\omega)e^{i\omega t} + \text{c.c.}) + \frac{1}{8}\chi^{(3)} \left| (A(\omega)e^{i\omega t} + c.c.) \right|^2 (A(\omega)e^{i\omega t} + c.c.) \Bigg). \tag{2.19}$$

By considering only effects at the laser frequency ω:

$$\begin{aligned} P &= \epsilon_0 \left(\chi^{(1)} + \frac{3}{4}\chi^{(3)} |A(\omega)|^2 \right) \frac{1}{2}(A(\omega)e^{i\omega t} + c.c.) \\ &= \epsilon_0 \left(\chi^{(1)} + \frac{3}{4}\chi^{(3)} |A(\omega)|^2 \right) \tilde{E}(t) \\ &= \epsilon_0 \chi_{eff} \tilde{E}(t). \end{aligned} \tag{2.20}$$

Using Eq. 2.17, this produces a refractive index

$$n = \sqrt{1 + \chi^{(1)} + \frac{3}{4}\chi^{(3)} |A(\omega)|^2}. \tag{2.21}$$

One can then expand the above equation to order $|A(\omega)|^2$:

$$\begin{aligned} n &= \sqrt{1 + \chi^{(1)}} + \frac{3\chi^{(3)}}{8\sqrt{1 + \chi^{(1)}}} |A(\omega)|^2 \\ &= n_0 + n_2 I, \end{aligned} \tag{2.22}$$

where n_0 is the linear refractive index:

$$n_0 = \sqrt{1 + \chi^{(1)}}, \tag{2.23}$$

and n_2 is the nonlinear, intensity dependent refractive index:

$$n_2 = \frac{3}{4n_0 \Re(n_0) \epsilon_0 c} \chi^{(3)}. \tag{2.24}$$

2.6 Self-Phase Modulation

In fibers, a primary effect of interest is self-phase modulation (SPM), where a pulse changes the phase of its own electric field through the nonlinear response of the refractive index. It can be mathemetically derived by considering the propagation of an optical pulse centered at frequency ω_0:

$$\tilde{E}(z,t) = \frac{1}{2} A(z,t) e^{i(\omega_0 t - k_0 z)} + \text{c.c.}. \tag{2.25}$$

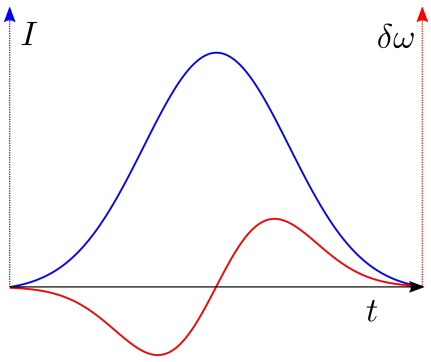

Figure 2.5: For a pulse with gaussian intensity envelope, the leading (left) edge is shifted down in frequency and the trailing (right) edge is shifted up.

The phase of the oscillation is modified by the refractive index:

$$\begin{aligned}\phi(t) &= \omega_0 t - k_0 z \\ &= \omega_0 t - \frac{\omega_0(n_0 + n_2 I)}{c} z.\end{aligned} \tag{2.26}$$

Next, we define the instantaneous frequency within the pulse $\omega(t)$:

$$\omega(t) = \omega_0 + \delta(\omega) = \frac{\mathrm{d}\phi(t)}{\mathrm{d}t}, \tag{2.27}$$

where $\delta\omega$ is the variation in the instantaneous frequency. The effect on the laser frequency after some propagation length L is simply:

$$\begin{aligned}\omega(t) &= \frac{\mathrm{d}\phi(t)}{\mathrm{d}t} = \omega_0 - \omega_0 L \frac{n_2}{c} \frac{\mathrm{d}I}{\mathrm{d}t} \\ \delta\omega(t) &= -\omega_0 L \frac{n_2}{c} \frac{\mathrm{d}I}{\mathrm{d}t}.\end{aligned} \tag{2.28}$$

For pulsed light, Eq. 2.5 shifts the frequencies of the leading and trailing edges of the pulse (Fig. 2.5), and can create new spectral components that were not present in the initial pulse. This also results in a positive chirp, as new lower frequency components precede the higher frequency ones. In the absence of other nonlinear effects such as Raman scattering, SPM creates symmetric spectral peaks flanking the original spectral peak [25].

2.7 Optical Solitons

With visible light, most materials exhibit normal dispersion. That is, the group velocity of red light is faster than blue light. When combined with the effect of SPM (which produces a similar effect), this leads to either pulse breakup or temporal broadening which limits further SPM.

In the infrared, substances like fused silica instead have anomalous dispersion, where longer wavelengths travel slower than shorter. This counteracts the effects of SPM and leads to what are called optical solitons. In an ideal medium with only SPM and anomalous GVD, these pulses maintain a periodic temporal shape for infinite propagation lengths. In real media, solitons are disrupted by higher order dispersion, stimulated Raman scattering, and fiber losses, but they are still able to support solitons over finite distances.

To understand the effects of solitons, it is useful to first define the dispersion length L_D and the nonlinear length L_{NL} in a particular fiber [25]:

$$L_D = \frac{T_0^2}{|\beta_2|} \qquad\qquad L_{NL} = \frac{1}{\gamma P_0}, \tag{2.29}$$

where T_0 is the half-width pulse duration at the $1/e$ intensity, P_0 is the peak power of the pulse, and γ is the effective nonlinear coefficient. These values provide length scales over which material dispersion (L_D) or nonlinear effects (L_{NL}) become relevant for pulse evolution.

For fiber lengths $L \ll L_{NL}$ and $L \ll L_D$, the pulse travels through the material mostly unchanged. For $L \ll L_{NL}$ and $L \sim L_D$, the pulse is mostly affected by GVD. Depending on the signs of the pulse chirp and the material dispersion, this can cause either a shortening or a lengthening of the pulse. For $L \ll L_D$ and $L \sim L_{NL}$, evolution is dominated by SPM, which produces new spectral components. When $L \sim L_D$ and $L \sim L_{NL}$, the interaction of GVD and SPM produces complex effects on the pulse. In the anomalous dispersion regime this often comes in the form of soliton formation, so it is useful to introduce the soliton number N:

$$N^2 = \frac{L_D}{L_{NL}} = \frac{\gamma P_0 T_0^2}{|\beta_2|}. \tag{2.30}$$

The soliton number determines the temporal oscillation pattern of the resulting soliton. For $N = 1$, this produces a constant sech^2 intensity envelope. Higher order solitons ($N > 1$) have periodic, oscillating temporal and spectral envolopes.

2.7.1 Raman Scattering

To properly characterize the evolution of solitons, it is necessary to also consider the delayed nonlinear response, specifically the resulting Raman effect. A CW "pump" laser which experiences the Raman effect has a portion of its spectrum shift to the red, called the Stokes wave [24]. Pump photons are converted into lower energy Stokes photons through excitation of a molecular vibrational state, and the energy difference is carried away in the vibration (i.e. optical phonon). The phonon/photon interaction can also create a blue-shifted anti-Stokes wave, but this is much less efficient that the Stokes wave. Generally, this spontaneous Raman scattering is very weak.

For strong pump powers, a significant number of Stokes photons can be produced. The successive beating between the pump and Stokes waves creates oscillations at the phonon frequency, which further excites the molecular vibration and causes Raman scattering to become much more efficient. This is called stimulated Raman scattering (SRS).

SRS in ultrashort pulses has a similar effect to the CW case, gradually shifting the spectrum to the red. However, GVD causes the red-shifted portion of the spectrum to move at a different group velocity than the pump pulse, and is thus referred to as the Raman pulse [25]. Resulting GVM between the Raman pulse and pump pulse eventually causes pulse splitting and limits the interaction length of SRS.

2.7.2 Soliton Formation

When an input pulse of soliton number $N_i \geq 1$ is sent into an anomalous dispersion fiber, a complex series of events begins. SPM begins to broaden the spectrum and produce blue- and red-shifted peaks, and the red-shifted portion becomes a seed for SRS [29]. This intrapulse Raman scattering creates a Stokes wave which can propagate as a "Raman soliton". As this process continues, the Raman pulse shifts further and further red as the red portion of the soliton spectrum seeds cascading SRS. This is called the soliton self-frequency shift [30].

In addition to the Stokes wave centered at frequency $\omega_0 - \delta\omega$, an anti-Stokes wave forms at $\omega_0 + \delta\omega$. Due to the relative inefficiency of the anti-Stokes wave, this phenomenon is usually negligible. However, if the anti-Stokes wave forms in the normal dispersion regime of the fiber, it can phase match four-wave mixing between two pump photons, a Stokes photon, and itself [31]. This FWM can drastically increase the power in the anti-Stokes dispersive wave. The resulting spectrum depends strongly on the dispersion profile of the fiber, which is often characterized by the zero-dispersion wavelength (ZDW). This value can be tuned via doping and waveguide dispersion, and can be used to vary the frequencies of the Stokes and anti-Stokes pulses via the phase matching condition.

2.8 The Generalized Nonlinear Schrödinger Equation

Understanding the complexity of supercontinuum generation in optical fiber requires more detail than SPM and GVD. To accurately determine the spectral evolution of broadband, high peak power pulses, one must also consider higher-order dispersion, SRS, and self-steepening among other effects [32]. This led to the development of a generalized nonlinear Schrödinger equation (GNLSE), which usually has no analytical solutions and must be calcu-

lated numerically. One form of the GNLSE commonly used in fiber supercontinuum simulations is,

$$\begin{aligned}\frac{\partial A}{\partial z} = &-\frac{\alpha}{2}A - \left(\sum_{n\geq 2}\beta_n \frac{i^{n-1}}{n!}\frac{\partial^n}{\partial \tau^n}\right)A + i\gamma\left(1+\frac{1}{\omega_0}\frac{\partial}{\partial\tau}\right) \\ &\times\left((1-f_R)A|A|^2 + f_R A\int_0^\infty h_R(T)|A(z,\tau-T)|^2 dT\right),\end{aligned} \tag{2.31}$$

where α is the attenuation constant and β_n are the coefficients of n^{th} order dispersion around the center frequency ω_0. f_R is the fractional strength of the delayed Raman response, and $h_R(t)$ is the Raman response function. Importantly, the above formula uses the sign convention common in physics:

$$\tilde{E}(z,t) = \frac{1}{2}A(z,t)e^{i(kz-\omega t)} + \text{c.c.}, \tag{2.32}$$

as opposed to the convention used previously in this section (see Eq. 2.4). Many code libraries exist to solve the GNLSE. In this thesis, we use a slightly tweaked version of Gabriel Ycas's PyNLO [33].

Chapter 3

Broadband Fiber Laser with Arbitrary Repetition Rate

3.1 Introduction

3.1.1 Mode-locked Lasers

The advent and successive proliferation of actively mode-locked lasers in the 1960s and 70s gave researchers the first access to consistent pulsed light sources on the tabletop scale [34]. These systems used synchronized electronics to modulate the laser cavity and create nanosecond pulses at repetition rates below 100 kHz.

The pursuit of shorter pulses, broader bandwidths, and higher repetition rates culminated in the development of the passively mode-locked oscillator (PMLO) in the early 1990s [35]. PMLOs use "saturable absorbers" (SAs) to enforce pulsed operation by increasing the loss for CW modes. This enables femtosecond pulses by removing the reliance on relatively slow electronics. Many PMLOs leverage the mature semiconductor manufacturing process to create semiconductor saturable absorber mirrors (SESAMs) [36, 37]. Other PMLOs use nonlinear optical effects as artificial saturable absorbers. PMLOs can also be made incredibly compact and stable by using optical fibers doped with a variety of rare-earth ions (e.g. erbium, thulium, ytterbium, and holmium) as gain media. Modern stabilization and fabrication techniques have produced PMLOs capable of few-femtosecond pulse durations, repetition rates of $\sim$10 GHz, and attosecond timing jitter [38, 39].

Femtosecond lasers based on PMLOs have a multitude of unique applications, including ranging [40], remote sensing [41], and machining [42] in addition to the more predictable time-resolved spectroscopy [43] and microscopy [44]. Passively mode-locked oscillators are particularly notable for their ability to create broadband frequency combs when phase stabilized, which was awarded part of the Nobel Prize in 2005 [45–47].

Adjusting the pulse repetition rate can benefit many applications that rely on the stability of the pulse trains produced by PMLOs. Changing the spacing

of frequency comb teeth is useful for metrology and spectroscopy, and lowering the duty cycle can produce higher peak powers in downstream amplifiers for nonlinear optics. However, passive mode locking provides a mostly static repetition rate.

Designing a PMLO for femtosecond pulses is a delicate process, and requires consideration of nonlinearities, pulse dispersion, cavity losses, etc. While perturbative intracavity modulations can enable slight alterations of the pulse repetition rate, substantial changes are usually not possible with the oscillator alone. Instead, pulse picking is usually performed downstream with external modulators.

3.1.2 The Nonlinear Erbium:fiber Amplifier

Er:fiber lasers and amplifiers are ubiquitous in the telecommuncations industry, where the 1550 nm emission of erbium is leveraged to transmit data through long fused silica fibers with minimal loss. This popularity has produced a plethora of inexpensive, high-performance commercial components. Despite decades of well-funded engineering, Er:fiber lasers have been slow to replace existing Ti:Sapphire and Yb laser systems. This is due in part by their limited spectral bandwidth, longer pulses, and poor power scaling.

However, many solutions now exist to broaden and shift the narrow bandwidth, including nanowaveguides [48] and small core fibers [49, 50]. Additionally, power scaling can be achieved using Er:Yb co-doped fibers, which use the higher absorption cross section of Yb^{3+} ions to improve 980 nm pump absorption.

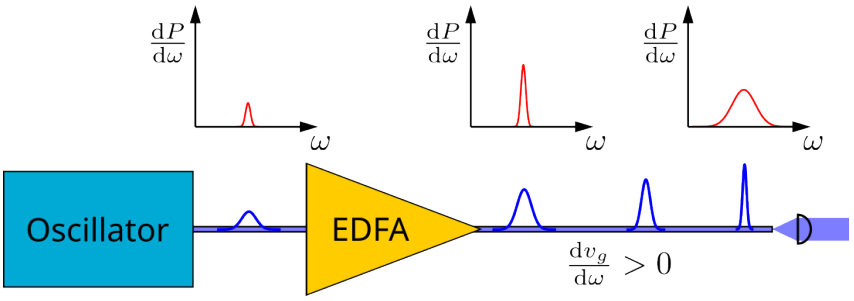

Figure 3.1: Narrowband light from an Er:fiber oscillator is amplified in an Er:doped fiber amplifier. The higher power drives SPM in a following fiber length, broadening the spectrum as it propagates. If the fiber is anomalous dispersion, soliton dynamics also temporally compress the pulse.

Despite the slow adoption, Er:fiber lasers can provide a robust, compact, and inexpensive platform for many fields of optical science. For example, modelocked Er:fiber oscillators can form the backbone of pump-probe spectroscopy [51], metrology [52], and nonlinear optics [53].

The foundation of these experiments is the nonlinear Er:doped fiber amplifier (EDFA). The nonlinear interactions required to generate broad bandwidths

and short pulses require stronger fields than many commercial oscillators can provide, and thus the pulses need amplification and temporal/spatial compression prior to frequency conversion. Shown in Fig. 3.1, the all-fiber nonlinear EDFA first uses a strongly pumped EDFA to amplify the pulse train to several nJs [53,54]. An ensuing length of single mode, anomalous dispersion fiber simultaneously generates new spectral components and compresses the pulse via soliton-effect compression [55].

These nonlinear EDFA schemes use a combination of SPM and dispersion to achieve ultrashort, high-energy pulses. This delicate balance is optimized only in a narrow range of EDFA pump power, seed power/chirp, and fiber lengths. Due to the nonlinear nature of the spectral broadening and compression processes, minor changes in any of these parameters can have dramatic changes in the resulting pulse shape.

Pulse Picking a Nonlinear EDFA

The sensitivity of nonlinear EDFAs introduces a difficult dilemma when pulse picking, as changing the input duty cycle of a nonlinear EDFA would nominally upset the delicate balance of SPM and dispersion, e.g., by changing the per-pulse EDFA gain [56]. This would disrupt the compression as in Fig. 3.2 B.

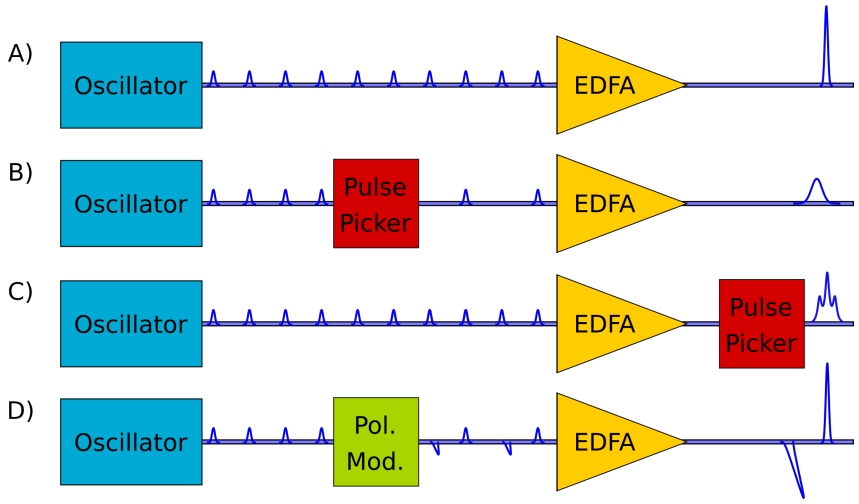

Figure 3.2: A) A properly tuned nonlinear EDFA produces compressed pulses at the repetition rate of the oscillator. B) Pulse picking prior to the EDFA changes the power of the pulses in the compression fiber, which do not optimally compress. C) Pulse picking after the EDFA can destroy the modulator or significantly alter the pulse shape. D) Modulating the polarization prior to the EDFA maintains the optimal compression and enables polarization-dependent pulse picking after compression.

Pulse picking after the EDFA (Fig 3.2 C) is also problematic. The high peak intensities within the compression fiber are capable of destroying delicate

waveguide modulators. Modulators capable of handling high peak intensities are not ideal either, as the crystals involved can induce strong nonlinearities in the pulse that break it apart. While it is certainly possible to couple into free space to increase the mode size and decrease the intensity, this is lossy and alignment-sensitive. If one is to keep the apparatus all-fiber, direct pulse picking is not an option.

Our solution is to modulate the polarization state of the light entering the EDFA (Fig. 3.2 D). This maintains the same per-pulse gain and preserves the pulse's initial conditions at the beginning of the compression fiber regardless of the repetition rate. Therefore, the desired pulses are optimally compressed at the end of the fiber, and undesired pulses can be removed with a polarizer or polarization-sensitive nonlinearities.

The relatively low peak power and narrow bandwidth prior to the nonlinear EDFA enable the use of fiber-coupled, compact, and highly efficient waveguide EOMs. Typically made possible by lithium niobate thin films, these EOMs use the Pockels effect to induce a phase shift in the light field when a voltage is applied across the film. Their miniature size also creates very low capacitances and enables several GHz switching speeds. Waveguide EOMs come in a variety of packages, notably as a polarization switcher or as a 1x2 Mach-Zehnder interferometer. Both of these configurations would function well to modulate the EDFA, but Mach-Zehnder routers tend to allow higher switching speeds.

3.1.3 Spectral Broadening in Highly Nonlinear Fibers

One can produce even broader bandwidths by launching the compressed, high-energy pulses from nonlinear EDFAs into small-core, highly nonlinear fibers (HNLFs) [49]. These smaller waveguides boost the strength of the optical electric fields by spatially compressing the light, which produces even more dramatic nonlinear effects. Similar to photonic crystal fibers (PCFs), deliberate dispersion engineering from variable doping and waveguide shapes can produce broad, precisely tailored spectra [50]. The combination of nonlinear EDFAs and HNLFs can generate octave-spanning bandwidths that can be recompressed to <5 fs [57]. They also see broad applications as a low-noise seed to Ho/Th amplifiers [58–60], OPAs [61] and OPOs [52]. The fiber-delivered nature of nonlinear EDFAs also means that these HNLFs can be spliced directly to the output port of the compression fiber, which grants the typical benefits of an all fiber platform (i.e. long-term stability and alignment insensitivity) for free.

Many HNLFs are made of solid fused silica. This makes them much easier to splice to standard silica fiber than highly structured PCFs. They also come is several distinct forms. Most are single-mode, with core sizes of a few microns. Recent developments have produced commercially available, birefringent, polarization-maintaining versions with elliptical cores [62].

When it comes to spectral broadening, the most important choice is the dispersion characteristics of the HNLF. Normal dispersion and anomalous dis-

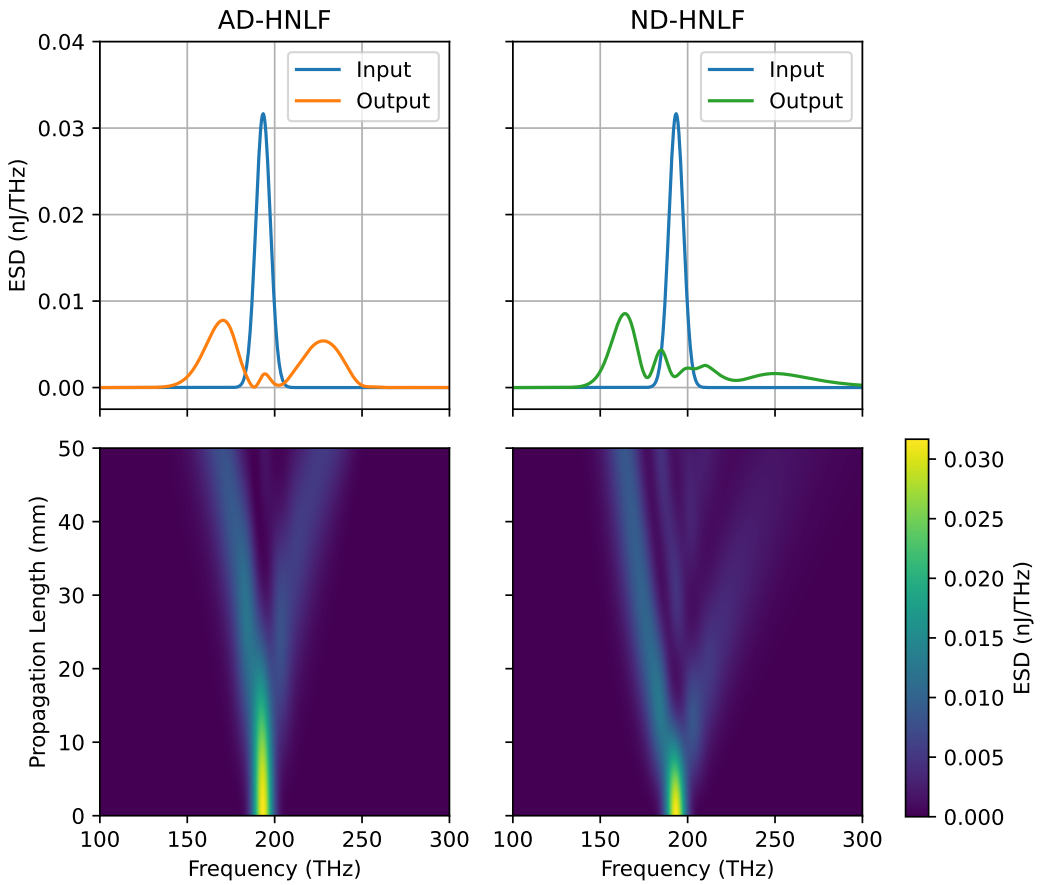

Figure 3.3: Simulated spectral generation by an unchirped, 45 fs gaussian pulse using PyNLO [33]. After propagating through 5 cm of anomalous dispersion (left) and normal dispersion (right) HNLF, the pulse produces characteristic spectra at the output. The anomalous dispersion (AD-HNLF) forms a Raman shifted soliton and blue-shifted dispersive wave around the pulse's initial wavelength. If it instead propagates through a normal dispersion fiber (ND-HNLF), several peaks are formed flanking the initial wavelength (right).

persion fibers produce drastically different spectral features from SPM and/or soliton/dispersive wave formation (see Sections 2.6 and 2.7 for more detail). Generally, the spectra appear as in Figure 3.3, where ND-HNLFs produce several peaks around the initial wavelength and AD-HNLFs produce a distinct pair of peaks: a red-shifted Raman soliton and blue-shifted dispersive wave [25].

3.1.4 Laser Noise

Whether through acoustic vibrations, electronic noise, thermal drifts, or amplified spontaneous emission (ASE), noise inevitably finds its way into all laser systems [63]. Laser noise comes in two main forms: phase noise and

intensity noise. Phase noise appears as a variation in the pulse-to-pulse phase of the E-field, but also as noise in the repetition rate/timing. Intensity noise, as the name keenly suggests, is the periodic fluctuations of the laser *power* and is the topic of the rest of this section.

The time-varying power output from a laser $P(t)$ can represented as:

$$P(t) = \bar{P} + \delta P(t), \tag{3.1}$$

where $\bar{P}$ is a constant average power and $\delta P(t)$ is the time-varying part with a mean of 0. It is then useful to consider the Fourier transform of $\delta P(t)$, here written as $\delta P(f)$. This quantity describes the frequency-resolved power fluctuations in $P(t)$. Instead of the absolute intensity noise $\delta P(f)$, it is more practical to quantify the *relative* intensity noise (RIN). Convention, however, demands that the RIN does not actually refer to the relative laser power $\delta P(f)/\bar{P}$, but instead to the relative detector power, or the laser power squared, $\delta P(f)^2/\bar{P}^2$. In this convention, the RIN can be written as a one-sided power spectral density [37]:

$$\text{RIN} = S_I(f) = \frac{2}{\bar{P}^2}\int_{-\infty}^{+\infty} \langle \delta P(t)\delta P(t+\tau)\rangle \, e^{i2\pi f\tau}\mathrm{d}\tau. \tag{3.2}$$

Most commonly, RIN is given logarithmically in dBc/Hz, the relative power to the DC "carrier" in a 1-Hz bandwidth [64]. For pulse trains, this carrier is actually centered at the laser repetition rate f_{rep}, but measurements of the noise usually alias this down to DC for f_{rep} in the several MHz. Calculating the root-mean-squared relative noise on the interval $[f_1, f_2]$ is then a simple calculation:

$$\left.\frac{\delta P}{\bar{P}}\right|_{\text{rms}} = \sqrt{\int_{f_1}^{f_2} S_I(f)\mathrm{d}f}. \tag{3.3}$$

3.2 Broadband Fiber Laser

3.2.1 The Erbium-Doped Fiber Amplifier

Following the general nonlinear EDFA design depicted in Figure 3.1, the backbone of the experiment is an Menlo Systems FC1500-ULN that provides a low-noise, 1550 nm pulse train at 60 MHz. While this oscillator platform enables a proper frequency comb, we do not perform the necessary frequency stabilization as that degree of precision is unnecessary for our application. Menlo oscillators have repeatedly demonstrated the ability to serve as robust oscillators for a variety of experiments [27, 53, 65]. On our particular unit, we observe significant SPM in the output fiber from the oscillator. When sent directly into an EDFA, we observed significant pulse breakup, and thus we cut the spectrum of the output with a 1565±3 nm bandpass filter. This not only cuts the power (and thus SPM), but also reduces the spectral bandwidth.

This results in a more stable pulse which can propagate through meters of fiber without substantial changes to its shape.

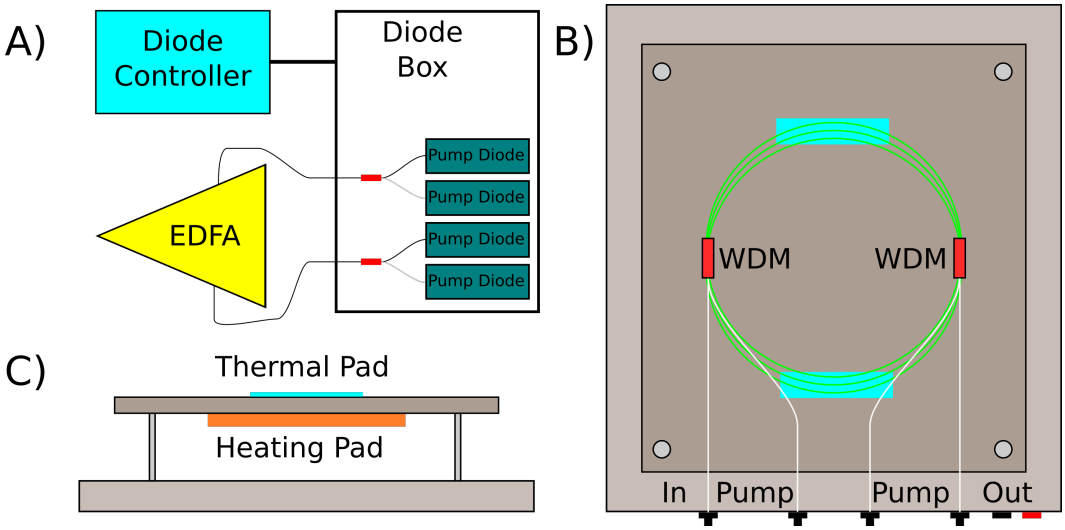

Figure 3.4: A) A controller module sets the pump diode currents and temperatures, and optionally takes direct user input or computer commands over the RS-232 serial bus. Pairs of pump diodes are combined at orthogonal polarizations and sent to the EDFA. B) Top view of the EDFA box. 980 nm pump light is coupled into the gain fiber (green) with a pair of wavelength-division multiplexers. The gain fiber rests atop several thermal pads to improve thermal contact with a metal plate. C) Side cross-section of EDFA box. A heating pad controls the temperature of the gain fiber, which slightly modifies its refractive index.

Component	Part #
WDMs	AFW WDM-PM-1598-L-P-7-2-1W
Gain Fiber	nLight Er80-4/125-HD-PM
Pump Diodes	3S 1999CVB
Pump Combiners	G&H FFP-5M3178G10
Pump Diode Controller	ILX Lightwave LDC-3916
Pump Diode Box	ILX Lightwave LDM-4616
Pump Diode Drivers	ILX Lightwave LDC-3916376
Passive Fibers	AFW PM 980 Patchcord

Table 3.1: Components in the home-built EDFA.

About 1 mW of the aforementioned pulses are eventually sent to a home-built nonlinear EDFA which is constructed entirely from readily available commercial components. The amplifier itself is a compact box (see Fig. 3.4 B and Tab. 3.1). A pair of wavelength-division multiplexers (WDMs) (1550 nm pass/980 nm reflect) allow 980 nm pump light to pass into the erbium gain

fiber, which is spliced directly to the WDM pigtails to minimize connector loss and fiber lengths.

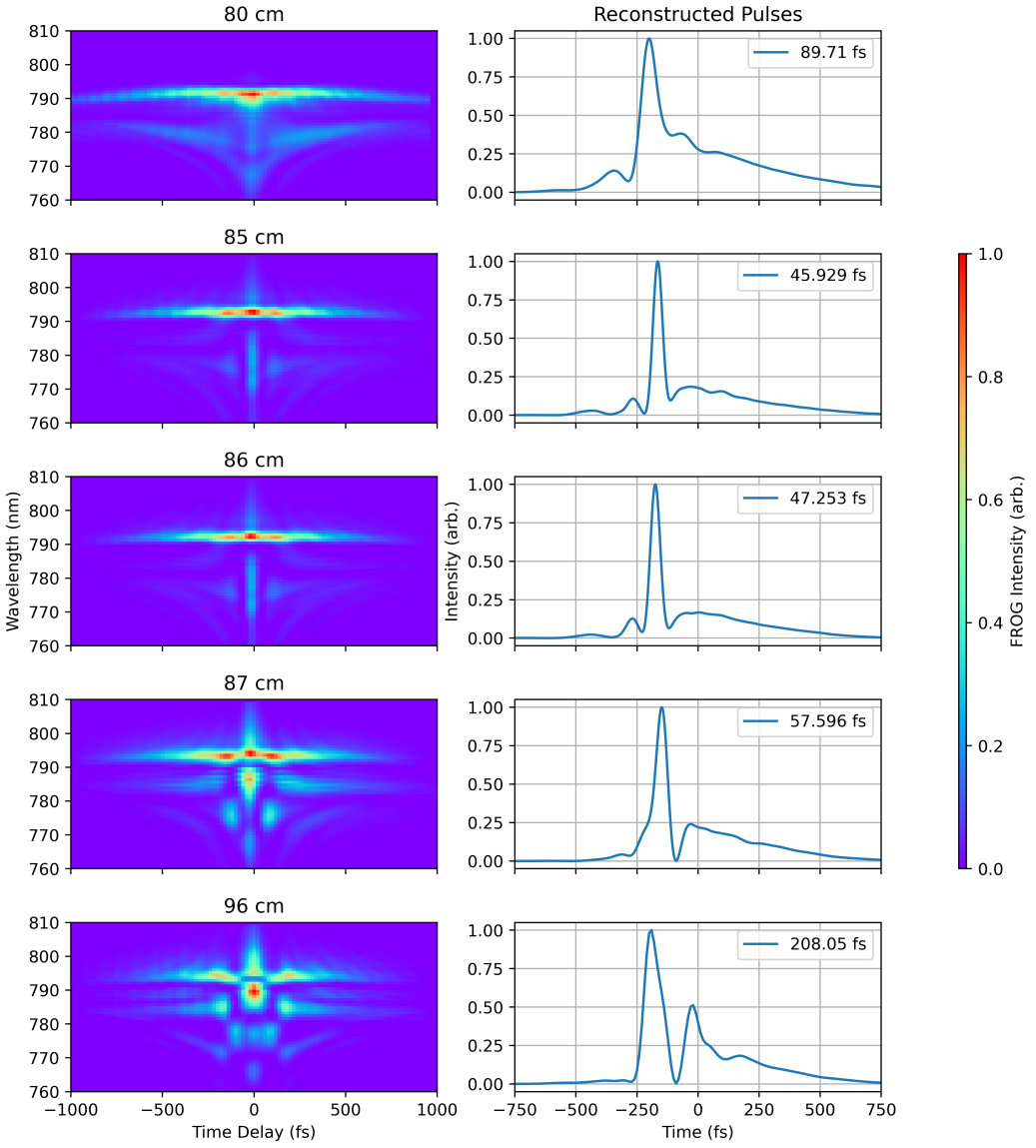

Figure 3.5: Measured SHG-FROG traces and reconstructed pulse envelopes used to find the optimal post-EDFA fiber length at constant pump power. Fiber lengths are labeled by the total length after the gain fiber.

The pump diodes take advantage of the simple, yet elegant, ILX Lightwave diode mainframe sketched in Figure 3.4 A. The controller is remote-controllable via its RS-232 interface, which allows for full integration of EDFA control into our existing software. Each mainframe contains room for up to 16 individual diode modules, meaning that up to 4 EDFAs can be driven from a single device. Indeed, the EDFA which generates our 1035 nm dispersive wave for the Yb:fiber amplifier is driven with the same mainframe. Each

pump diode outputs linearly polarized light, so we combine them in pairs at orthogonal polarizations to avoid the complexity of coherent combination.

The final aspect of the amplifier is its temperature control (Fig. 3.4 C). The gain fiber rests on several thermal pads that improve thermal contact with a thin metal plate. This plate has a 20 W heating pad attached beneath it, and is separated from the chassis with set screws to reduce the thermal mass and improve response time. This temperature control modulates the refractive index of the gain fiber, thus changing the time delay of the output pulses. For more detail on the servo controls, see Section 5.1.1.

Optically, the EDFA performs well, and amplifies 1 mW of input light to >350 mW when pumped with 600 mW of light from each of the four 980 nm diodes. To find the optimal length of compression fiber, we connected PM 1550 pigtails of various lengths to the output of the EDFA and measured the pulse duration with a home-built SHG-FROG [66]. The nonlinear EDFA's sensitivity to the initial conditions required us to include the ∼4 dB loss of the polarization modulator during the optimization process. To minimize the number of variables, we kept pump powers at a steady 600 mW each, and only varied the fiber length. When preceded by the 1565 ±3 nm bandpass filter, the EDFA produces stable, compressed pulses which reach their minimum pulse duration of 45 fs with 84.5 cm of PM 1550 fiber after the gain fiber (see Fig. 3.5). The bandpass filter succeeds in reducing the sensitivity to dispersion (i.e. fiber lengths) prior to the gain fiber, as the addition of several meters created no noticeable effect on the compression. These fiber lengths are recorded in Table 3.2.

While the necessity of splicing means that measuring the soliton number is not possible in the fiber immediately after the gain fiber, we know that by the end of the compression fiber, $L_D = 3.2$ cm, $L_{NL} = 6$ mm and $N = 2.3$. This firmly places us in the realm of soliton-effect compression [55].

Location	Length - EDFA chassis (cm)
Before Gain Fiber	64
Gain Fiber	150
After Gain Fiber	43
Location	**Length - Total (cm)**
Before Gain Fiber	>300
After Gain Fiber	85

Table 3.2: Lengths of PM 1550 fiber in the laser.

3.2.2 Spectral Broadening in Highly Nonlinear Fibers

HNLF Splice Construction

We launch the compressed pulses from the nonlinear EDFA into an assortment of HNLFs to further broaden the spectrum. In order to achieve the full

fiber delivery, the HNLFs must be spliced directly to PM 1550 fiber. There are many parameters to vary when creating an HNLF splice:

HNLF Dispersion As discussed in Section 3.1.3, the choice of normal vs. anomalous dispersion has an enormous effect on the shape and bandwidth of the spectrum. Additionally, the specific dispersion curve has more subtle effects, especially the ZDW of anomalous dispersion fibers.

HNLF Length The longer the interaction regime, the more time there is for nonlinear interactions. At the same time, this also gives more time for the pulse to break up.

PM 1550 Length Even if one were to extremely precisely determine what length of compression fiber produces the shortest pulse, it does not necessarily produce the best spectrum.

Splice Recipe The splice recipe plays an huge role in the amount of light which is successfully coupled into the core of the HNLF, as well as how well aligned the light is to the fiber axes.

All of this is to say that creating an HNLF splice is a trial-and-error process, and our data was collected with the best performing splices. The ND-HNLF dispersion is -2.6(slow)/-0.8(fast) ps/(nm·km) at 1550 nm. The AD-HNLF is 2.2/1 ps/(nm·km) at 1550 nm. Both of these fibers are custom runs of OFS's elliptical core, polarization maintaining, 4 μm mode field diameter fiber. Our splice recipe (initially from OFS and then optimized by us) splices the slow axis of PM 1550 to the fast axis of the HNLFs. Given the issues with the fast axis of the PM 1550 highlighted in Sec. 3.3.2, all of the following data will use the fast axis of the HNLF unless otherwise stated.

Spectrum Generation

It is helpful to first analyze how the HNLF behaves indepedently of repetition rate variations. Figure 3.6 compares the the spectra created by the two HNLFs to the light as it makes its way through the system, and the effect of the HNLF is immediately clear. Although the compression fiber alone produces a bandwidth of ∼100 nm, the anomalous HNLF creates a supercontinuum and the normal dispersion HNLF creates ∼600 nm of bandwidth.

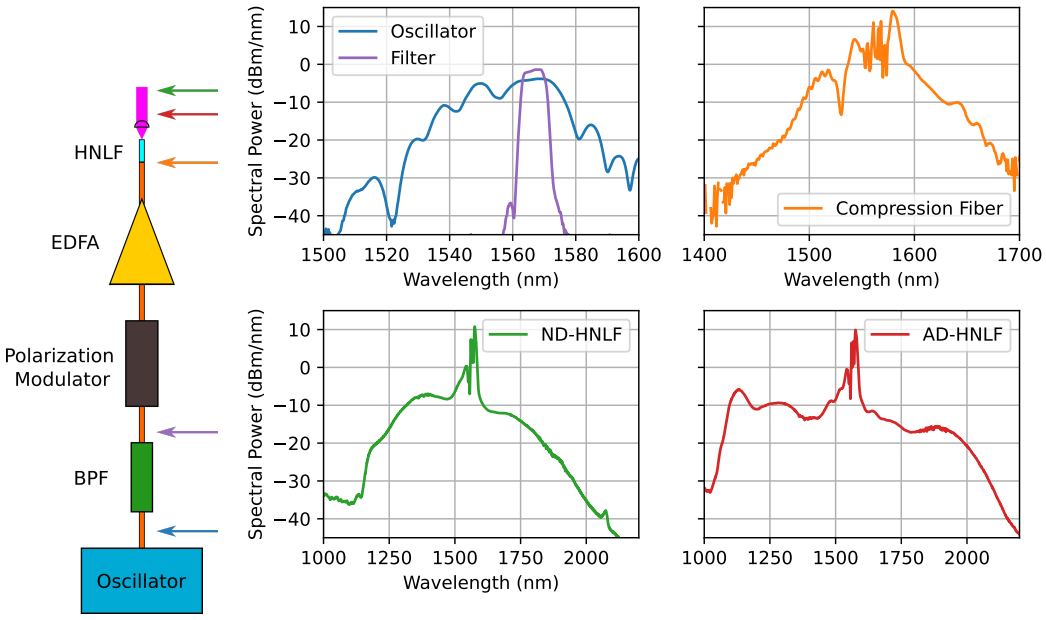

Figure 3.6: (left) Simplified diagram of the modulated nonlinear EDFA + HNLF scheme. (right) Spectrum of the light at various points indicated on the diagram. Spectra at the end of the compression fiber and each HNLF were collected at the full laser repetition rate.

For the ND-HNLF, we see the characteristic SPM peaks flanking the center spikes around 1400 nm and 1700 nm. The AD-HNLF spectrum is more structured, with a clear dispersive wave forming around 1100 nm and a corresponding Raman soliton around 1900 nm.

3.3 Achieving Arbitrary Repetition Rate

3.3.1 The Modulation Scheme

Our implementation of tunable repetition rate aims to maintain the same per-pulse EDFA gain using the polarization modulation scheme illustrated in Figure 3.7 (parts list in Table 3.3). After the 1565±3 nm bandpass filter, pulses from the Er:fiber oscillator are programmably routed to two parallel fibers using a lithium niobate electro-optic 1x2 Mach-Zehnder interferometer. The EOM supports a pair of inputs for independent control of the DC offset and RF pulses. Both ports are driven by a HP 8110A pulse generator. What distinguishes the 8110A is the option to directly clock it at 60 MHz, which we do with a fast photodiode to minimize timing jitter. It is also capable of outputting 10 V peak-to-peak square waves. Although the V_π quoted by the modulator is nominally only a few Vs, in practice we need to use 8.35 V_{pp} pulses since we are driving with frequencies far below the intended few-GHz regime of the modulator. Even when optimized, the pulser produces adverse

effects on the pulse contrast and laser noise which are discussed further in Sections 3.3.2 and 3.3.5.

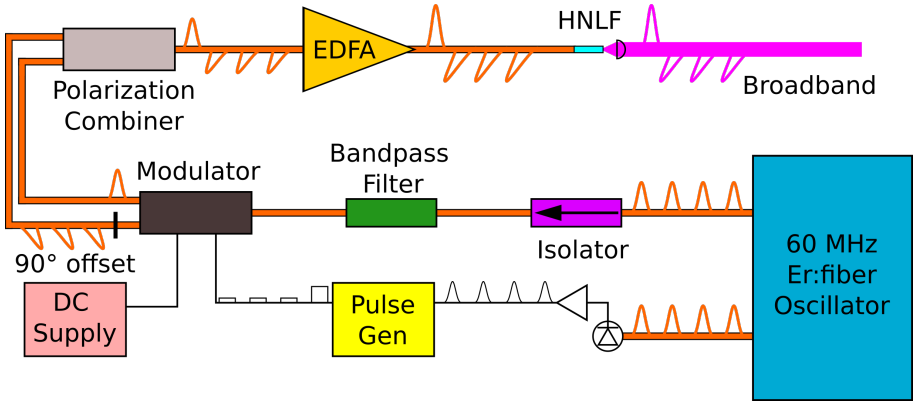

Figure 3.7: Light from an erbium oscillator triggers a pulse generator to synchronously produce an arbitrary electric pulse pattern. An electro-optic modulator writes this arbitrary pattern onto the linear polarization state of the oscillator. This modulated light is amplified in a nonlinear EDFA, then launched into an HNLF to generate broadband IR light.

The two outputs of the modulator are then combined in a polarization beam combiner, with one arm having a 90° twist which switches the linear polarization of undesired pulses from the slow axis to the fast axis. Minute differences in the fiber lengths of the two arms also creates a ∼100 ps timing offset. The combination of delay and polarization offset allows for pulse picking with timing and/or polarization-sensitive nonlinearities (e.g. sum-frequency generation), or even a simple polarizer. Importantly, while the following data and analysis prefers to use a constant, reduced repetition rate (as this is by far the most practical use case), this modulation scheme allows completely arbitrary selection if which pulses to pass. This includes schemes with irregular pulse spacing.

Component	Part #
Oscillator	Menlo Systems FC1500-ULN
Isolator	AFW PISO-2-15-FB
Bandpass Filter	Haphit FPBP-1565-60-H03P1-2L10-FC/APC
Modulator	EOSpace AX-1x2-0MSS-10-PFA-PFA
Polarization Combiner	Thorlabs PFC1550A
EDFA	See Sec. 3.2.1
AD-HNLF	OFS 1 ps/(nm·km) (fast axis) PM-HNLF
ND-HNLF	OFS -0.8 ps/(nm·km) (fast axis) PM-HNLF
Passive Fiber	AFW PM 1550 Patchcord
Pulse Generator	HP 8110A
DC Supply	HP 8110A

Table 3.3: Parts list for the broadband, arbitrary repetition rate laser.

The polarization-modulated pulse train is then sent to our home-built nonlinear EDFA for amplification and compression. The compressed pulses are then sent directly into a connectorized HNLF splice, which lets us easily vary the splice parameters to dial in optimal spectra.

3.3.2 Pulse Contrast

The polarization state of the light throughout the system is not perfect, despite the usage of birefringent, polarization-maintaining fiber. The dominating limitation is the EOM itself. For any given pulse from the oscillator, two pulses are created in the parallel fibers afterward, i.e. the left side of Fig. 3.7. This gives us a pair of pulses on orthogonal polarizations, although one (the main pulse) is much stronger than the other (the stray pulse). At the output of the combiner, we observe a on/off pulse contrast of ∼17 dB on the slow axis (see Fig. 3.8). This performance is comparable to the polarization contrast specification of the modulator itself (18 dB). Lastly, minute differences in fiber lengths of the two arms cause the pair of pulses to emerge from the polarization combiner with a distinct temporal separation. For our batch of components, they are separated by ∼150 ps.

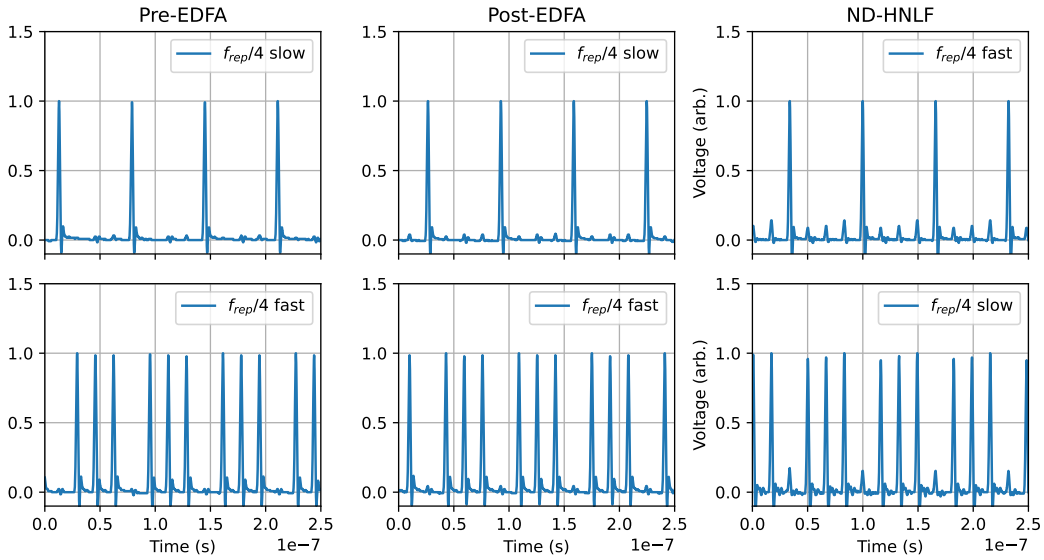

Figure 3.8: Photodiode voltages of the pulse train along the slow and fast PM 1550 fiber axes as well as the HNLF. Note that our splice takes light from the slow axis of the PM 1550 to the fast axis of the HNLF. The pulse-to-pulse contrast decreases steadily as the pulses pass through the modulator (left), nonlinear EDFA (middle), and HNLF (right), from 17 dB to 15 dB to 10 dB. The contrast of broadened light in the HNLF is better than 10 dB.

The next degradation comes from the amplifier and compression fiber, after which the slow axis pulse contrast falls to 15 dB. This is partially a side-effect of

the imperfect pulse routing. Since the stray pulses from the modulator are almost two orders of magnitude less powerful than the main pulses, they remain in the small-signal gain regime of the EDFA longer, and are proportionally amplified more than the main pulse. Additionally, as the pulse duration drops in the compression fiber, nonlinearities like cross-phase modulation (XPM) become relevant.

XPM, like SPM, relies on the nonlinear refractive index n_2. However, instead of acting on the pulse itself, it creates cross-talk between two or more pulses. XPM does not cause interaction between the main and stray pulses due to the timing delay, rather the two orthogonal polarization states of the main pulse. This results in a nonlinear polarization evolution as the pulse propagates [25].

This XPM effect is likely the primary cause of the subsequent drop in contrast after the HNLF. Since the HNLF has a much smaller core, the strength of XPM scales alongside the SPM and/or soliton formation we are actually trying to induce. Additionally, the act of splicing a large, circular core fiber to a small elliptical core fiber certainly induces further degradations. Although the spectrally integrated contrast is only 10 dB, the contrast of broadened light is much better, as discussed in Section 4.2.6. Still, the presence of rejected pulses along the incorrect axis means that this configuration strongly benefits from other nonlinear or spectrally selective interactions to improve the contrast.

Also discussed in Section 4.2.6, the timing separation of the two arms means that stray pulses are not actually an issue for our OPA. However, the XPM effects have no such timing separation and can cause issues with the pulse contrast downstream.

Lastly, there is a consistent variation in the pulse-to-pulse intensity, which is most obvious in the HNLF traces in Figure 3.8. This is due to RF ringing in the transmission cables between the pulser and modulator. This can be improved by using shorter cables or with better impedance matching.

3.3.3 Pulse Compression

Figure 3.9 shows selected pulses at the end of the compression fiber at different modulation duty cycles. The nonlinear nature of the SHG-FROG measurement drastically increases the signal to noise, and lets us to isolate selected pulses at relatively low repetition rates. The duration of the main pulse is approximately 45 fs independent of the duty cycle, even at repetition rates as low as $f_{rep}/10000 = 6$ kHz.

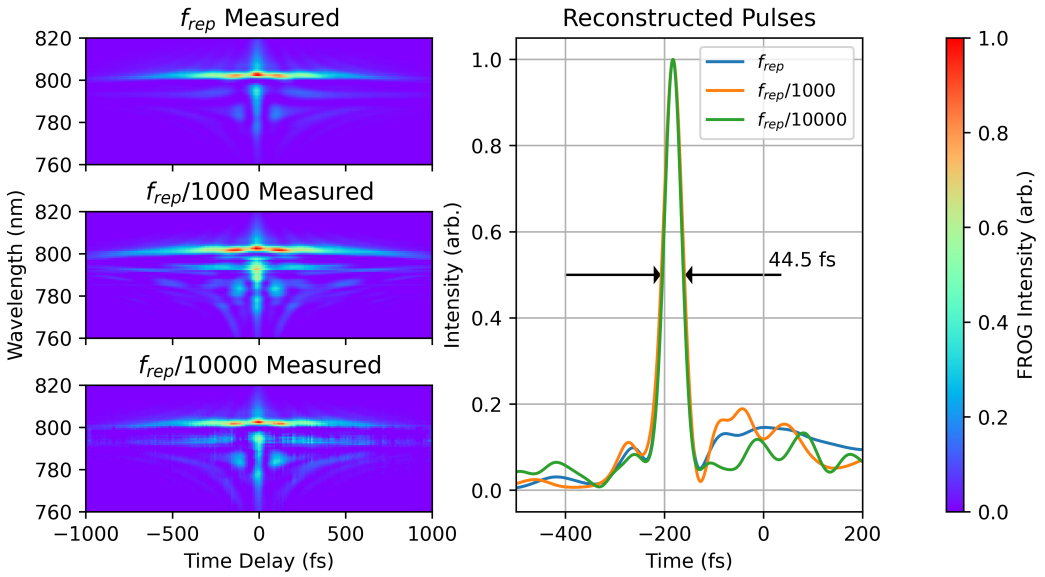

Figure 3.9: Pulse reconstructions of SHG-FROG traces taken with optimized fiber lengths along the PM 1550 slow axis. The pulse shape is largely independent of repetition rate, with added noise coming mostly from background signal in the measurement confusing the reconstruction algorithm.

Interestingly, this duty cycle independence is not present on the fast axis of the PM 1550. Even at repetition rates as low as $f_{rep}/5$, it is clear just by the FROG traces that the pulses are not only different, but also are valid FROG traces. This data can be found in Figure A.1 in the appendix. It is unclear what causes this behavior, and is a topic of further investigation.

3.3.4 Spectrum Generation

The pulse shape is extremely sensitive to the initial conditions, and the spectrum is itself highly dependent on the pulse shape. The most important benchmark for our application is whether or not the spectrum remains consistent independent of the repetition rate. Fortunately, Figure 3.10 indicates that the pulse spectra along the fast axis of the HNLF stay mostly consistent as the repetition rate varies. The power spectral densities (PSDs) show an offset corresponding to the varying duty cycle, and the energy spectral densitites (ESDs) are nearly indistinguishable.

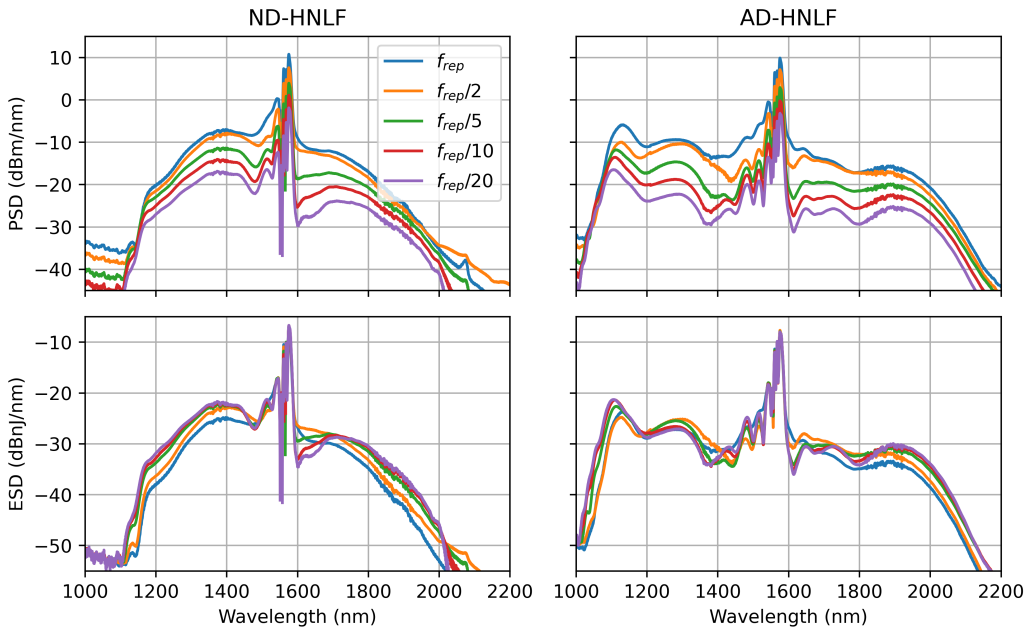

Figure 3.10: (top) PSD of light coming through the fast axis of the HNLFs. The spectra are mostly consistent, with only a slight vertical offset characteristic of a drop in duty cycle. (bottom) Energy spectral density calculated using the various repetition rates. The curves are very similar, indicating that the spectra of individaul pulses stay consistent. Light leaking through from rejected pulses is background subtracted proportional to the duty cycle.

3.3.5 Laser Noise

First are matters of convention. Since the average power is constantly changing with the repetition rate, the RIN normalization factor and the shot noise limit do as well. Therefore, the shot noise and background level are both calculated from the DC value of the weakest signal in the figure. Also, it is not always intuitive to compare RIN curves with different repetition rates, so this section also includes the raw, unnormalized detector data. Data in these figures is collected with a static attenuation, so the DC carrier decreases in proportion to the repetition rate.

We measured the noise of the laser at many different locations to see how different components affect the noise. It is important to first observe the inherent noise from the oscillator and EDFA without modulation, depicted in Fig. 3.11. The EDFA boosts the weak signal from the oscillator so much that the signal increase outpaces any additional noise, at least from 200 Hz-3 kHz.

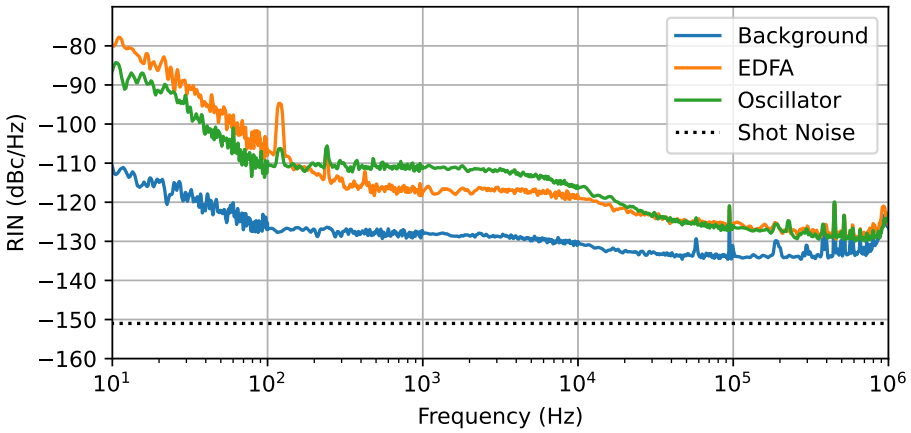

Figure 3.11: RIN of light directly out of filtered oscillator and at the end of the unmodulated EDFA compression fiber.

The next consideration is the EOM, which has the potential to write significant RF noise onto the optical signal. Figure 3.12 compares the RIN and raw noise for slow axis light at multiple repetition rates directly out of the polarization combiner, where each RF pulse passes an optical pulse. Corresponding fast axis data, where each RF pulse blocks an optical one, is included in the appendix (see Fig. A.2).

At frequencies less than 10 kHz, the raw noise is comparable for all repetition rates. The RIN values deviate, but this is only due to the reduced signal. This seems to imply that the noise floor in this regime comes from unpolarized ASE in the oscillator. Finding the cause of the strange pattern above 10 kHz first requires attenuating the 60 Hz harmonics.

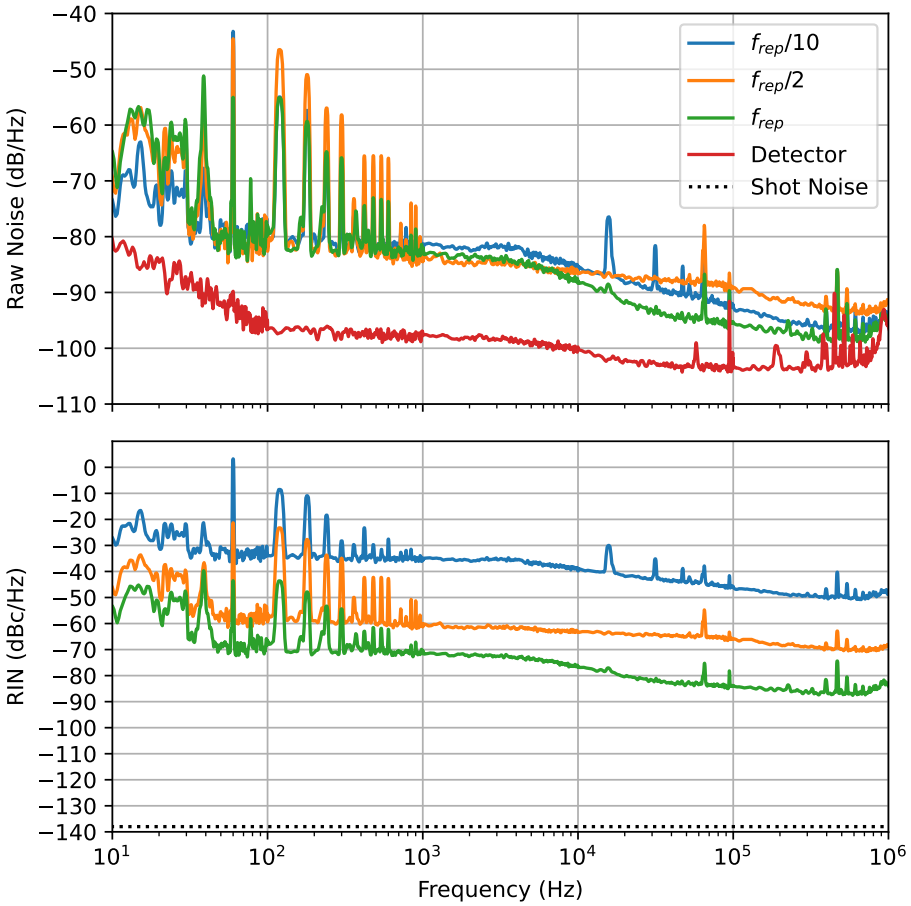

Figure 3.12: RIN and raw detector data of slow axis light without the nonlinear EDFA.

The last step is to add the EDFA after the modulator and observe its effects. Slow axis data are shown in Figure 3.13 (fast axis in Fig. A.3). Once again, the RIN drops with increasing repetition rate. The only noticeable additional effects of the amplifier are to reduce the RIN across the board and to slightly distinguish the raw noise in the <10 kHz region.

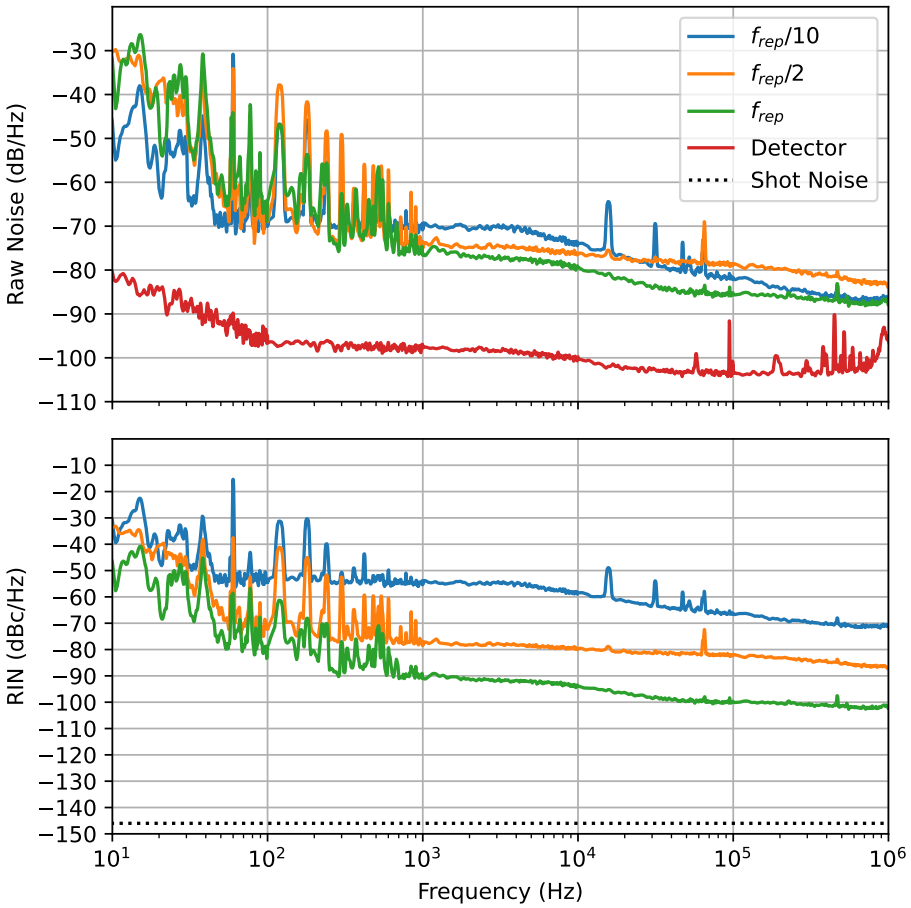

Figure 3.13: RIN and raw detector data of amplified slow axis light at the end of the compression fiber.

There are two main takeaways from this data. First, the total noise in the power of the laser shows no clear pattern with the repetition rate, but the total power decreases proportionally to the repetition rate. This means that the RIN drops roughly proportional to the increase in repetition rate.

Second and more obvious, there are massive spikes at 60 Hz and its harmonics. Clearly, this is mostly technical noise from the modulator, which in turn receives this noise from the voltages applied to it. Reducing this noise is a matter of improving electronics. The noise from the DC port can be solved by using a battery, but the pulses on the RF port produce most of the noise. This is clearly visible in Figure A.3, where the pulser is nominally not pulsing at f_{rep}. There are still 60 Hz peaks from the DC and RF, but they are dramatically reduced in magnitude. It may be possible to reduce the magnitude of these spikes by using a better pulser or by properly AC coupling the RF port of the modulator. This is still a work in progress.

This noise analysis is useful to have for the broadband femtosecond fiber laser as a standalone product, but the noise figures matter little for the intended application. The low electron counts of our low-fluence TR-ARPES

produce shot noise limits in excess of -20 dBc/Hz.

Chapter 4

From Broadband Infrared to Tunable 660-800 nm

4.1 Introduction

4.1.1 Laser-Induced Crystal Damage

The efficiencies of nonlinear optical processes depend strongly on the magnitude of the electric field in the interacting beams. Increasing the strength of E-field increases the strength of the desired nonlinearities, but it also magnifies the probability of crystal damage mechanisms.

Crystal damage is often considered a threshold process. As such, it is useful to characterize a maximum value beyond which permanent damage is likely. For femtosecond pulsed lasers, a common metric is the peak pulse energy per unit area, or peak fluence. For gaussian beams, this is,

$$F = \frac{2U}{\pi w(z)^2} \tag{4.1}$$

Where U is the pulse energy and $w(z)$ is its $\frac{1}{e^2}$ beam size. When operating close to this threshold, maximizing the strength of nonlinear interactions (i.e. the amount of OPA gain or the SHG conversion efficiency) becomes a careful balance between reliability and performance.

An important caveat is that while the damage threshold for femtosecond lasers is generally well-defined by the fluence, it also has a complex relationship with the repetition rate and spectrum [67]. Thus, damage thresholds are more of a guideline, with direct comparison only meaningful when using lasers with similar repetition rates and wavelengths.

For lasers with fluences of 1-10 mJ/cm^2 like our 10 W, 1035 nm pump laser, the characteristic damage mechanisms include avalanche breakdown and multi-photon absoprtion (MPA) [24]. As the name implies, MPA is the simulteous nonlinear absorption of multiple photons below a transition energy which nonetheless produces an electronic excitation. MPA can have several detrimental effects. If the MPA puts electrons in the conduction band of the

crystal, they begin to absorb broadband radiation (sometimes called inverse Bremsstrahlung) and cause crystal heating, burning, and/or cracking. MPA can also directly ionize atoms within the lattice, which can produce temporary or permanent changes to the refractive index and transmission [68].

Avalanche breakdown begins with a small number of free electrons in the conduction band, such as from MPA. These free electrons readily absorb all wavelengths of radiation, and rapidly accumulate high energies. When they impact other atoms within the lattice, they can impact-ionize them, producing more free electrons and causing a catastrophic feedback loop which further reduces the crystal transmission across the optical spectrum [24].

4.1.2 Damage Mechanisms of Lithium Niobate

Our OPA is centered around a periodically-polled lithium niobate (PPLN) crystal. Lithium niobate is an incredibly versatile crystal with several convenient optical properties. It is transparent from the visible well into the mid-IR, and thus for the complete range of wavelengths for both our OPA signal and idler. It is birefringent, and has an exceptionally high d_{eff} of 17 pm/V when used in QPM geometries. When fabricated with a periodic polling process, PPLN can form the foundation of high-gain amplifiers and efficient frequency converters [27, 69]. Lithium niobate's primary drawback in this context is its middling damage threshold of of ∼10-15 mJ/cm^2 when pumping with femtosecond Yb lasers at 60 MHz repetition rate [67].

The damage mechanism of interest is called green-induced infrared absorption (GRIIA), where the presence of visible green light increases the absorption of infrared radiation. Several explanations have been proposed for the physical origins of the phenomenon [67, 70, 71], but many can be traced back to a combination of avalanche breakdown and multi-photon absorption.

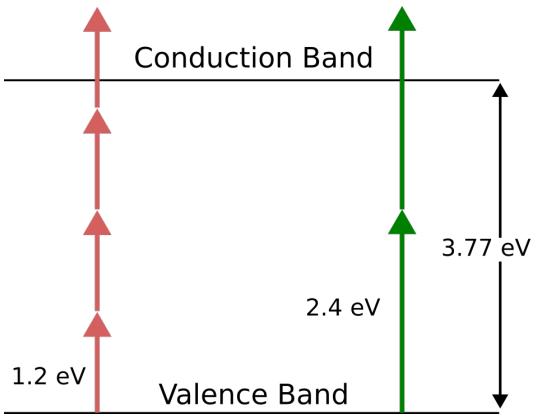

Figure 4.1: Instead of a low probability 4-photon absorption by the infrared pump, PPLN's high nonlinear gain produces enough second harmonic to create significant 2-photon absorption.

Lithium niobate has a bandgap of ∼3.77 eV at room temperature [72].

In typical conditions, the 4-photon absorption probability of our 1.2 eV pump photons is negligible, as the intensities required are enormous. However, PPLN has extremely high gain, which includes parasitic processes like SHG of the pump. Even without proper QPM, an OPA can easily produce enough green light for the probability of 2-photon absorption of the 2.4 eV second harmonic to become significant (see Fig. 4.1).

At higher intensities near the damage threshold, these conduction band electrons can begin the process of avalanche breakdown, and these free electrons also readily absorb the more powerful IR light. With small spot sizes, this localized heating can lead to severe and rapid ablation, burning, and cracking.

4.1.3 Alternative Systems

Other methods of creating ultrashort pulsed lasers with tunable visible wavelengths exist, such as synchronously-pumped optical parametric oscillators (SP-OPOs). SP-OPOs are already capable of producing tunable visible light and can be derived exclusively from relatively narrow bandwidth sources like Yb [65, 73].

The difficulty comes from the tunable repetition rate, as the cavity-enhanced nature of a SP-OPO means that the cavity signal's round-trip group delay must align with the pulse period of the pump. The minimum repetition rate supported by the SP-OPO cavity is thus defined by its geometry, with smaller minima requiring longer cavities.

Another option for producing tunable visible light is an OPA pumped with the second harmonic of Yb. Such a design could directly provide our desired wavelength tuning range of 650-900 nm [74], and would not suffer from the same arbitrary repetition rate struggles as a SP-OPO. In this case, crystal properties are the main limitation. As mentioned in 4.1.2, PPLN struggles with GRIIA, so directly pumping with green light is not ideal. PPLN also has very strong GVM in the visible which would limit the crystal length to less than a millimeter. While crystals such as lithium triborate (LBO) have higher damage thresholds and lower GVM at these wavelengths, they also have significantly lower d_{eff} ($\sim$ 1 pm/V for LBO).

Ultimately, the relative simplicity of using a NIR-based OPA is the main driving force in the decision. While the ability to directly produce visible light out of the OPA is tempting, we have already proven the ability of OPAs to produce several Watts of output power in the IR [27], and the technology to create broadband IR sources is well established [53]. The addition of SHG also helps to improve the pulse-to-pulse contrast.

4.2 Design and Performance

4.2.1 Optical Layout

The full diagram of the OPA is shown in Figure 4.2, with components in Table 4.1. 10 W of 1035 nm Yb light passes through a variable attenuator (a half-wave plate and polarizer) which lets us vary the output power independently of the repetition rate. The pump is focused to a spot size of approximately 50 μm ($1/e^2$ intensity) at the center of the PPLN crystal.

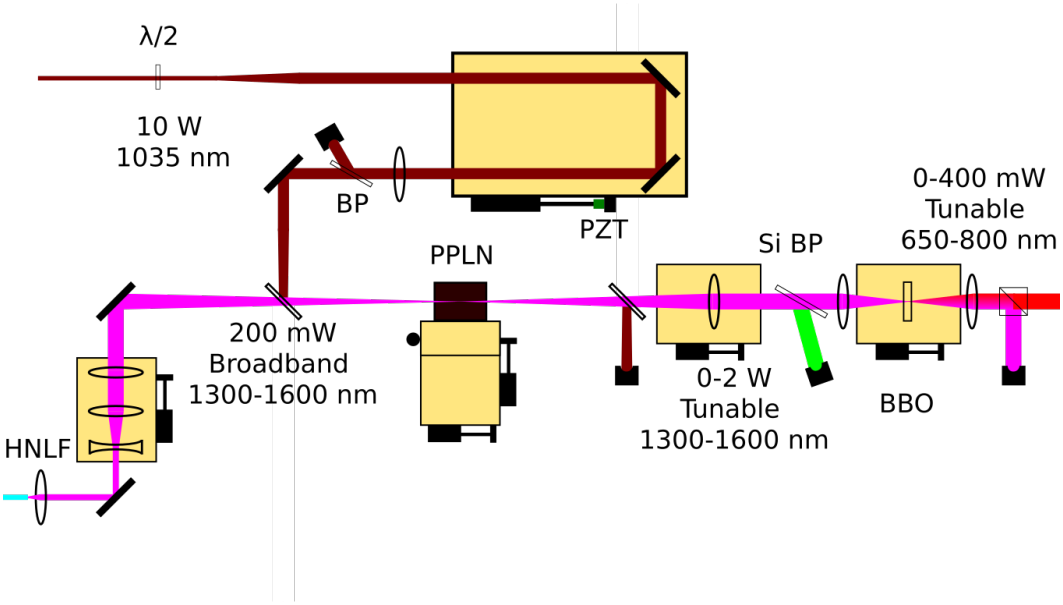

Figure 4.2: Optical layout of the OPA/SHG system. Light from the tunable seed collides in a PPLN crystal with 1035 nm pump light of adjustable power. Spatial and temporal overlap of the pulses can be adjusted with a trio of stages. The amplified signal is separated from residual pump with a dichroic mirror and a Si Brewster plate before entering a BBO for SHG.

In parallel, light from the arbitrary repetition rate seed (see Chapter 3) is broadened in a ND-HNLF and sent into free space with a fiber coupler. It then passes through a telescope and focusing lens to focus it to a waist of 40 μm ($1/e^2$) for overlap with the pump. Due to the strong SPM in the HNLF, the seed signal pulse emerges positively chirped. This means that changing the wavelength also requires slightly adjusting the temporal overlap.

A retroreflector is placed on a stage in the pump arm to precisely control the pump/signal timing. A piezoelectric transducer is integrated into the stage's micrometer to provide femtosecond precision in the temporal overlap. This PZT can also be used as a feedback device in future iterations of this setup (see Sec. 5.1.1).

The beams are combined with a dichroic mirror before entering the crystal with p-polarization. The PPLN is supported by a 3-axis stage, which allows

Component	Part #
Fiber Coupler	Thorlabs F240APC-1550
Signal Telescope Lens	Thorlabs LC1715-C
	Thorlabs LA1509-C
Signal Focusing Lens	Thorlabs LA4579-C
Signal Steering Mirrors	Thorlabs PF10-03-P01
Pump Focusing Lens	Thorlabs LA4579-B
Half-Wave Plate	Thorlabs WPH10M-1030
Brewster Polarizer	Altechna 2-BFP-1064-0254
Pump Steering Mirrors	Altechna 1-OS-2-0254-5-[1PR45]
Dichroic Mirrors	Laseroptik R-02140
Collimating Lens	Thorlabs LA1433-C
PPLN Crystal	HC Photonics 1BKML5G23159002123100Y001
	HC Photonics 1BKML5G22815003123100Y001
Silicon Brewster Plate	University Wafer A1246
SHG Focusing Lens	Thorlabs LA1608-C
BBO Crystal	Newlight BTC5100-21(I)-P
SHG Collimating Lens	Thorlabs LA4380-AB

Table 4.1: OPA Parts List

selection of the polling period (y), proper overlap of the crystal with the focus of the pump (z), and moving the crystal in and out of the beam line for alignment purposes (x). A similar stage on the focusing lens in the signal seed arm allows overlap of the signal focus once the crystal's z-stage is optimized.

Excess pump light is dumped out of the beam line with another dichroic, and the trasmitted amplified signal is collimated with a lens and then filtered by a silicon brewster plate. This wafer of silicon is opaque to wavelengths below 1100 nm, which further attenuates the 1035 nm pump light and eliminates parasitic visible light from the PPLN. At brewster angle, it also helps filter off any s-polarized light from the seed signal (such as rejected pulses). It is only 700 μm thick, but the strong dispersion of silicon requires it to be as thin as possible to maintain a temporally compressed pulse.

The amplified signal light is tightly focused into a BBO crystal in a rotation mount that grants continuous control of the phase matching angle. Second harmonic light is generated in the orthogonal s-polarization, and allows a polarizer to filter off the p-polarized fundamental.

4.2.2 Phase Matching

Since both second harmonic generation and optical parametric amplification are parametric processes, they are both limited in their effectiveness by phase matching.

OPA Quasi-Phase Matching

The OPA uses periodically poled lithium niobate (PPLN) as the nonlinear crystal, primarily because of its high parametric gain (d_{eff} = 17 pm/V) and transparency to both the signal and idler [28]. The pulse-splitting length due to GVM is about 2 mm, and the finite acceptance bandwidth (∼1 THz·cm across the signal spectrum) means that we need multiple discrete polling periods to cover the whole spectral region of interest.

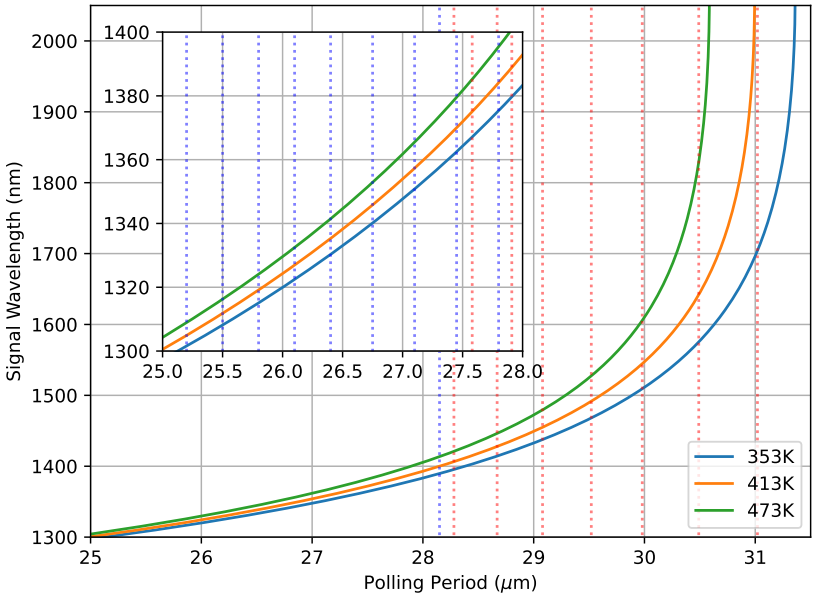

Figure 4.3: Curves of the OPA signal wavelength over a range of quasi-phase matching periods and crystal temperatures. Blue dotted lines signify polling periods on the 3 mm crystal, while red dotted lines delineate the 2 mm crystal.

We ultimately settled on a pair of crystals from HC Photonics: one 2 mm crystal with 10 discrete polling periods to cover the 1370-2000 nm spectral region, and a 3 mm crystal with another 10 discrete polling periods to cover the 1300-1370 nm region (Figure 4.3). These discrete polling periods can be temperature tuned to overlap with with each adjacent period, which allows continuous wavelength tunability. The discrepancy in crystal length is due the having less power in the seed spectrum in the 1300-1370 nm region (Fig. 3.6), which requires more amplification. This does have the side-effect of limiting the spectral bandwidth to 3.3 THz on the longer crystal, instead of 5 THz on the shorter crystal.

SHG Birefringent Phase Matching

For the second harmonic, we use β-barium borate (BBO) both for its optical properties and its simplicity. While it is possible to take advantage of PPLN's enormous d_{eff} and perform QPM to generate the second harmonic,

the bandwidth is comparatively narrow and the resulting pulses are ∼1 ps long [75]. The time resolution of TR-ARPES benefits from broad bandwidths and short pulses, so Type-I (o+o=e) birefringent phase matching in BBO is the logical choice.

Although it has a much smaller d_{eff} of 1.95 pm/V, it can be easily angle tuned across the entire wavelength region when the crystal is cut at $\theta = 21°$. The optimal phase matching angle varies by about 1° across the entire spectrum with a large acceptance angle, so once optimized, the angle hardly has to be changed, if at all. We use a 1 mm thick crystal that has more than enough bandwidth to cover the entire fundamental at each polling period.

4.2.3 Power Tunability

The arrangement of our OPA allows for variable attenuation of the 1035 nm pump, and we can use this to carefully dial in a desired second harmonic power (Fig. 4.4). The power in the second harmonic scales roughly linearly with the power of the fundamental. While we would expect the $\chi^{(2)}$ nature of SHG to produce a quadratic scaling, this behavior only manifests at low power where pump depletion is negligible.

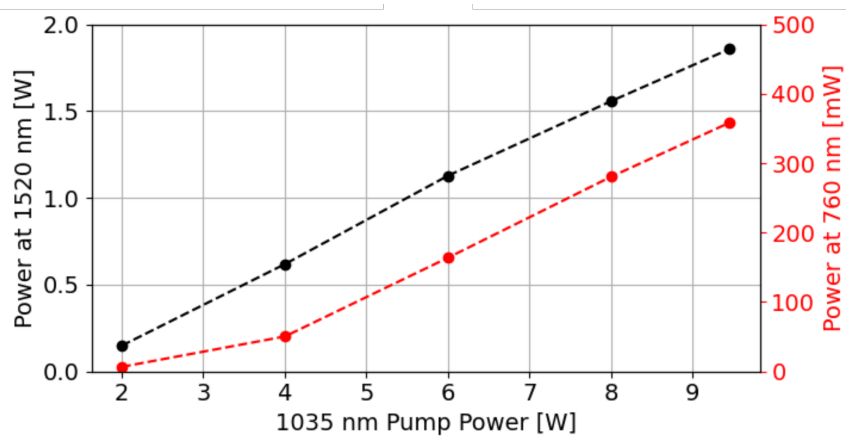

Figure 4.4: Power in the amplified 1520 nm fundamental (black, left) and the second harmonic (red, right) at various pump powers.

4.2.4 Wavelength Tunability

Seeding the OPA with the broadband HNLF signal allows us to amplify specific, few THz bandwidth chunks at a time. Figure 4.5 shows how the power in the fundamental IR and the visible second harmonic vary over the spectral region of interest. There is a sharp drop in power when moving to the 3 mm crystal, despite its increased gain relative to the 2 mm crystal. Unfortunately, GRIIA (see Sec. 4.1.2) limits the amount of pump power we can utilize for these wavelengths, as the longer crystal improves the efficiency of parasitic SHG of the 1035 nm pump. Still, we successfully produce about

half the amount of signal power as the 2 mm crystal while using about half the amount of pump power.

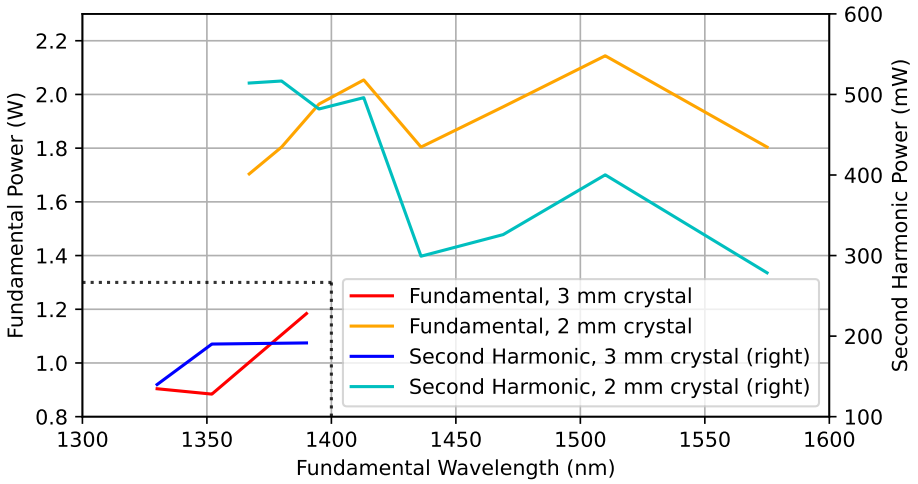

Figure 4.5: Power in the amplified signal (left) and second harmonic (right). The 2 mm crystal (orange, cyan) tunes over most of the spectral region of interest, and consistently handles 10 W of pump power. The 3 mm crystal (blue, red) only covers a narrow spectrum due to its proximity to the 1035 nm pump wavelength. Additionally, the lower power on the 3 mm crystal is due to limiting the pump power to 4-5 W.

The complex seed spectrum predictably produces complex spectra in the amplifier. As demonstrated in Fig. 4.6, this becomes more exaggerated closer to 1550 nm in the fundamental, where the SPM peaks in the seed spectrum are largest and most numerous (Fig. 3.6). These complex spectra also appear in the second harmonic, with transform limited pulse durations of about 100 fs. Notably, these spectra depend quite sensitively on the timing delay of the OPA. Moreover, the timing delay corresponding to maximum signal power does not always produce the least structured spectrum. This could make locking the timing delay more challenging if a more gaussian spectrum is desired.

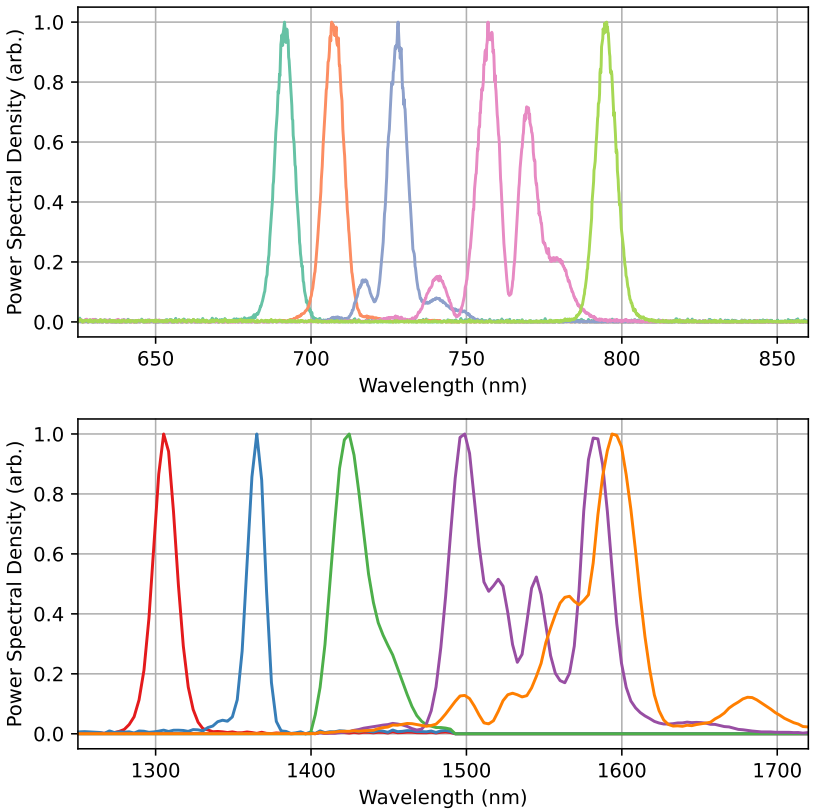

Figure 4.6: Fundamental OPA signal (bottom) and SHG (top) spectra over a range of QPM periods. Spectra near the fundamental 1550 nm are more structured due to the complex seed spectrum.

Beyond 1600 nm

GRIIA is a critical limitation when operating the OPA at high powers, and its effects are much stronger when phase matching for 1600-2000 nm signal. PPLN is also commonly used as a frequency doubler of 1035/1064 nm light due to its high d_{eff}, so even when it phase matches at higher orders (see Sec. 2.4.2), the conversion efficiency is high enough to cause problems.

The first order QPM period for SHG in PPLN is about 6 microns, the 5th order of which is right around the 1600-2000 nm signal regime (Fig. 4.7). Indeed, the reason that none of the previous data in this chapter includes wavelengths beyond 1600 nm is due to a dramatic increase in 517 nm intensity. This produces severe, consistent crystal damage when scaling the pump power. This issue is a topic of further research, and is addressed in Section 5.1.2.

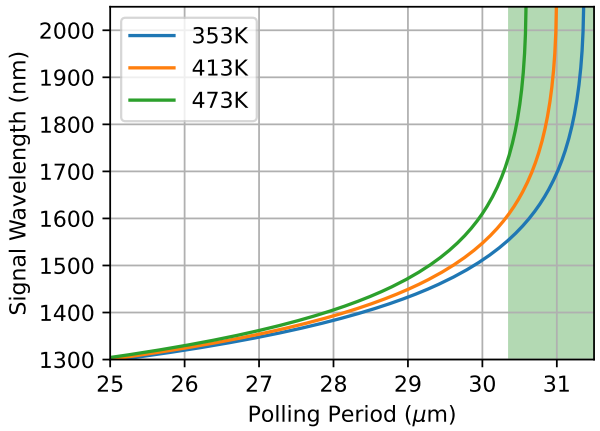

Figure 4.7: Phase matching curve for our PPLN crystal. The green highlighted region signifies where 5th-order SHG of the 1035 nm pump phase matches.

4.2.5 Spatial Mode Quality

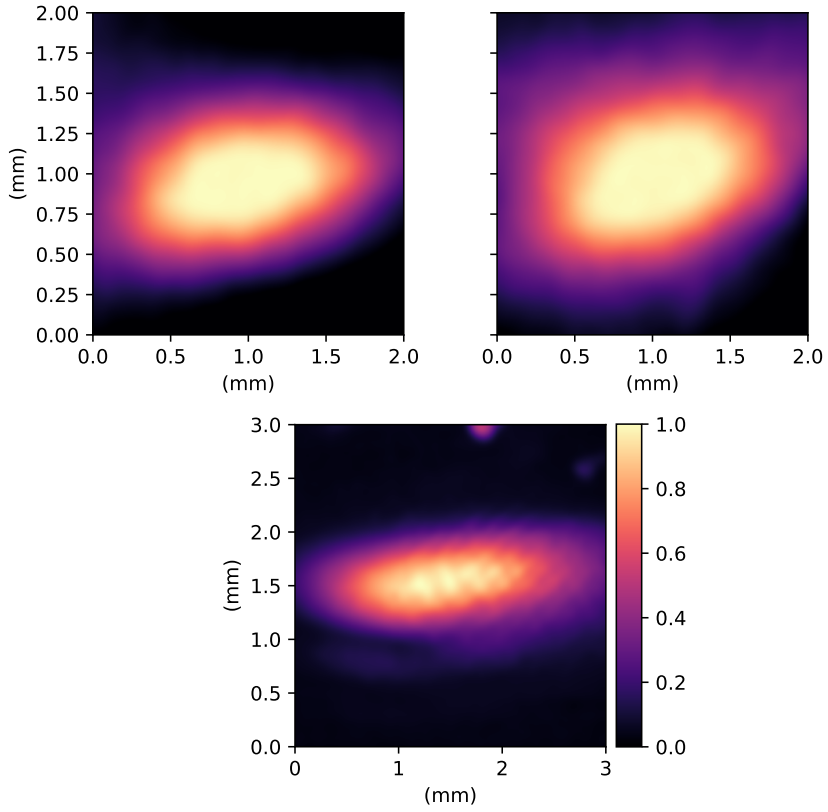

Figure 4.8: Spatial modes of the unamplified signal (top left), amplified signal (top right) and second harmonic (bottom).

We measured the spatial mode of the fundamental with a FLIR Boson LWIR thermal camera. The spatial modes of both the input signal and the pump shape the output signal's spatial profile. The unamplified signal has an elliptical profile reflecting the elliptical core of the HNLF from which it emerges, as depicted in Figure 4.8. The shaping effect of the pump is clear in the amplified signal. While it is still elliptical, it is rotated by about 10°. Importantly, it stays consistent while varying the repetition rate.

The mode of the second harmonic is more structured, and becomes still more elliptical. Sub-degree deviations in the phase matching angle of the BBO also create horizontal fringes which require careful alignment to eliminate. Even when tuned optimally by eye, the camera reveals a dim lobe beneath the primary spot (Fig. 4.8). Most likely this is due to complications of the phase matching condition due to tight focusing. This tight focusing causes incoming light to have a cone of k-vectors as in Fig. 4.9. The plane of light focused perpendicular to the plane containing the central k-vector and the optical axis sees no change in the phase matching condition By contrast, orthogonally focused light sees a varying θ depending on the distance from the center of the beam. This partially spoils the phase matching condition and reduces conversion efficiency. Put together, this forms a severely elliptical mode in the second harmonic.

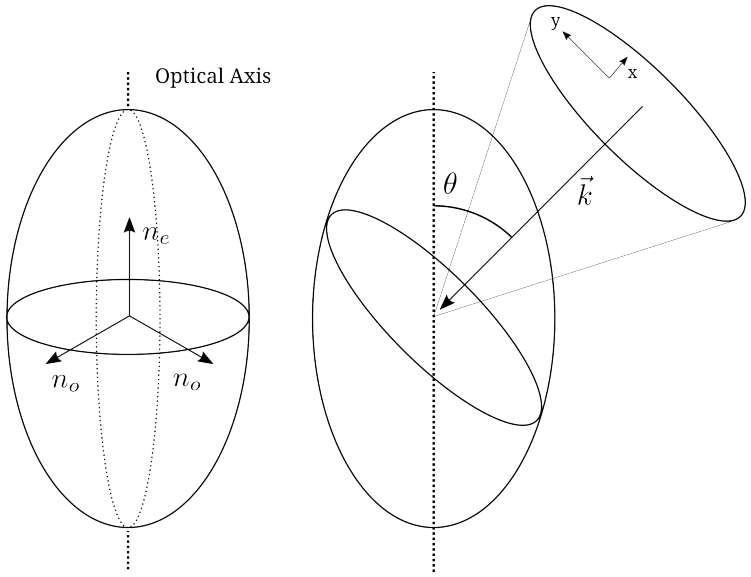

Figure 4.9: When light is tightly focused, it produces a cone of k-vectors near the focus. Light focused along the "x" axis still enters the crystal at angle θ from the optical axis, and sees no effect on the conversion efficiency. Light focused along the "y" axis enters the crystal at an angle different than θ, and this deviation increases the further away from the center of the beam. This causes a decrease in conversion efficiency.

4.2.6 Pulse Contrast

Light from passed pulses emerges from the HNLF in three ways depicted in Figure 4.10 A). Fortunately, only light on the fast HNLF axis with proper timing (shown in green) is amplified in the OPA. Nonlinear polarization rotation (NPR) arising from XPM (blue) and stray pulses (pink) create light along the slow axis of the HNLF and have no effect in the OPA.

Light from rejected pulses follow the same formula, and are shown in Figure 4.10 B). Again, only light on the fast axis with proper time (green) is amplified. However, the pulse is so weak and long that it receives little spectral broadening and will not be amplified if the OPA is tuned away from 1550 nm. NPR (purple) of light in the main pulse (pink) also contributes to the diminished 10 dB pulse contrast along the ND-HNLF fast axis in Figure 4.11.

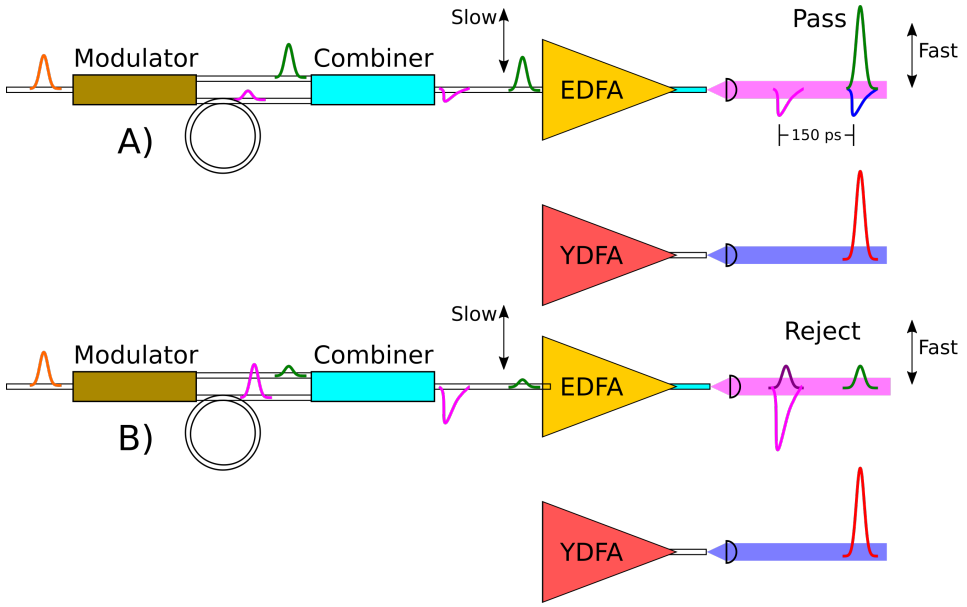

Figure 4.10: For every pulse from the oscillator, two pulses separated by ∼150 ps are created in the EDFA due to the unbalanced fiber lengths between the modulator and polarization combiner. Light that receives OPA amplification must have both the correct timing and polarization (green). A) When the green pulse is passed, it is much stronger, which broadens its spectrum to include the OPA QPM wavelength. B) When the green pulse is rejected, it is too weak and too spectrally narrow to interact if the OPA is not tuned to QPM 1550 nm, despite having proper polarization and timing.

However, when the OPA is is tuned away from phase matching 1550 nm (Fig. 4.11, top middle), the pulse contrast is clearly much better than 10 dB. When the OPA is set to phase match 1420 nm, the pulse contrast improves to 15 dB after amplification. When the OPA is tuned to phase match 1550 nm (Fig. 4.11, bottom middle), the pulse contrast *decreases* to 5 dB, as weaker rejected pulses experience more total gain. The effect of the RF ringing

discussed in Section 3.3.2 is also most visible here.

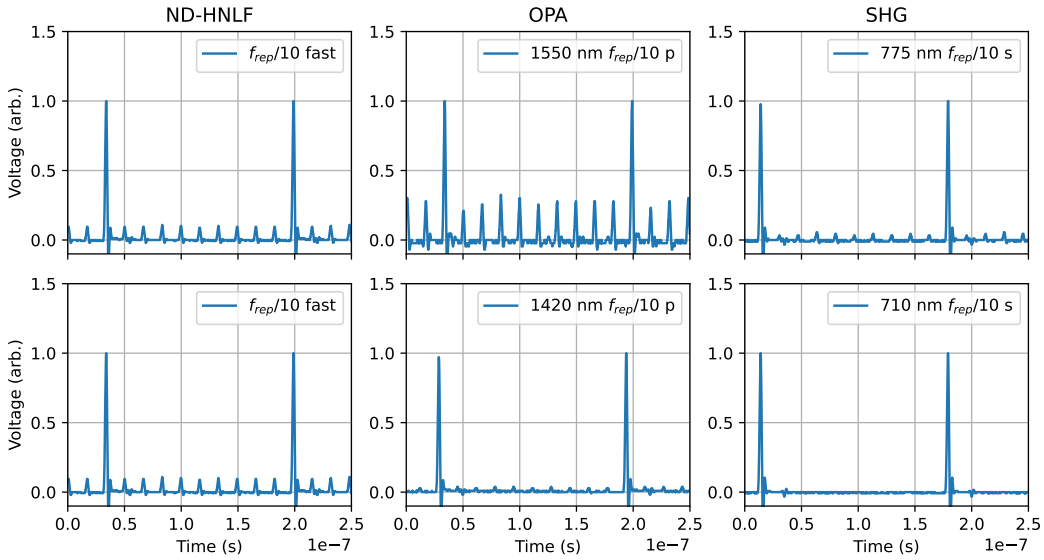

Figure 4.11: Photodiode traces of the polarized pulse contrast at the output of the HNLF (left), amplified by 10 W of pump in the OPA (middle), and converted to the second harmonic (right). Phase matching away from 1550 nm produces significantly better contrast throughout the system. Deviations in the pulse-to-pulse height is caused by RF ringing.

SHG significantly improves the contrast in both cases, as the efficiency scales quadratically with the peak intensity. In the worst case of phase matching 1550 nm fundamental, the second harmonic still reaches a respectable contrast of 14 dB. When phase matching 1420 nm fundamental, the pulse contrast is better than our oscilloscope can measure (i.e. >24 dB).

The measurement of the second harmonic also benefits from inherent spectral filtering. The measurements of the fundamental were performed with an InGaAs detector which is sensitive to nearly the full spectrum. The visible measurements require a silicon detector, which is transparent to wavelengths above 1100 nm (i.e. the fundamental). So, the spectrally-resolved contrast of the fundamental is actually better than the traces indicate, as much of the light in the rejected pulses is stray 1550 nm light. The SHG measurements are insensitive to this light, as the Si does not detect it.

Chapter 5

Conclusion

5.1 Next Steps

While the system succeeds in providing a laser of tunable wavelength and repetition rate, it falls short in a handful of categories that are enumerated below.

5.1.1 Active Stabilization

A tunable pump is a good start for unlocking new avenues for TR-ARPES, but this laser needs to be able to sustain stable operation for the many hour aquisition times of a typical TR-ARPES experiment. Most critically, the timing between the pump and signal of the OPA is sensitive to the femtosecond. Since there are several meters of propagation length in both the signal and pump arms, this delay is highly susceptible to temperature drifts.

The proposed locking scheme is modeled after the apparatus in Catanese et. al. [27] and is shown in Figure 5.1. A PZT fiber stretcher placed before the EDFA is driven at 1 kHz by the local oscillator of a lock-in amplifier. This modulates the delay of the signal on the order of femtoseconds. The delay modulation causes a matching modulation in the depletion of the pump:

$$I_{\text{out}}(t) \propto F\left(\tau + \alpha\cos(\Omega t)\right) \approx F\left(\tau\right) + \frac{\mathrm{d}F}{\mathrm{d}\tau}\alpha\cos(\Omega t), \tag{5.1}$$

where τ is the pump/signal delay, Ω is the modulation frequency, and $F(\tau)$ characterizes the pump intensity I_{out} at a given delay. When this voltage signal is returned to the lock-in, it generates an signal proportional to the coefficient of $\cos(\Omega t)$. This creates an error signal proportional to $\frac{\mathrm{d}F}{\mathrm{d}\tau}$ which we minimize to ensure optimal pulse overlap.

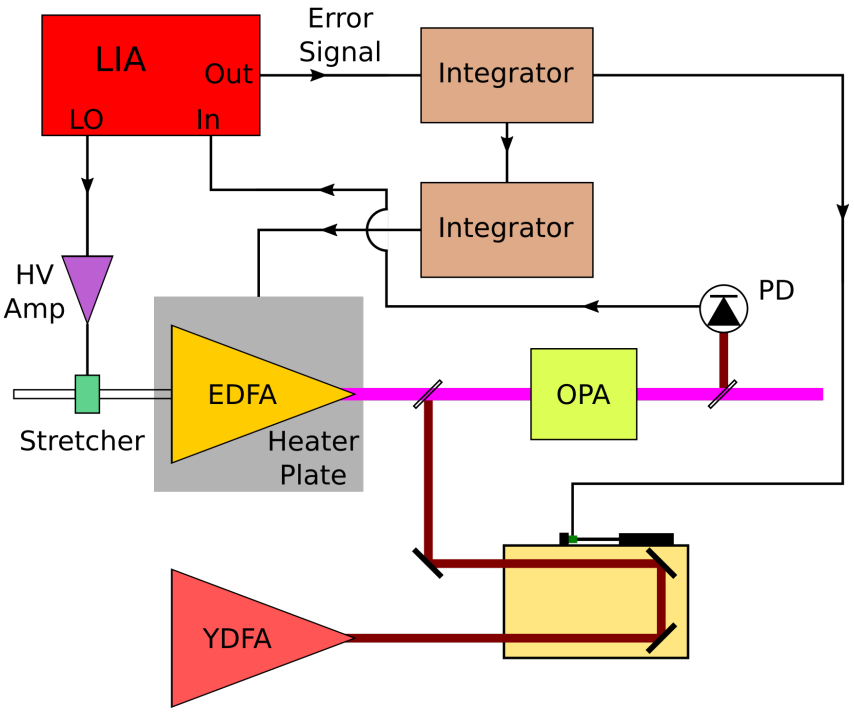

Figure 5.1: The local oscillator (LO) of a lock-in amplifier (LIA) is amplified to modulate the delay with a PZT fiber stretcher. This modulation is detected on a photodiode (PD) and allows the lock-in to generate an error signal. The error signal is integrated before driving feedback with a PZT in the delay stage. A second integrator uses the EDFA heater to servo the PZT to remain in the middle of its stroke.

The first component of the feedback loop is a PZT stage on the pump arm. This offers relatively fast feedback, but is limited to a short 15 μm stroke. Over the course of many hours, it is likely to exceed this limited feedback range.

To supplement the PZT, a fiber heater is integrated into the signal EDFA (see Section 3.2.1). This variable heating slightly changes the refractive index of the $\sim$2 m of fiber within the amplifier, and provides slow feedback. The fiber heater allows the PZT to stay within the center of its stroke while it performs higher frequency corrections.

5.1.2 Beyond 800 nm

The original goal of the tunable pump was continuous wavelength tunability from 650-900 nm. The current apparatus succeeds in the 660-800 nm range, but is unable to produce significant signal beyond that due the crystal damage effects discussed in Section 4.2.4. In the current geometry, this mandates finding a way to produce 1600-1800 nm signal light in the OPA.

The simplest option is to use a different crystal. Since different crystals have unique dispersions and refractive indexes, they also use different polling periods to phase match the same interactions. One potential option is potas-

sium titanyl phosphate, or KTP. Like LN, KTP can also be readily purchased with periodic polling, although with a lower d_{eff} of 9.7 pm/V in comparison to PPLN's 17.1 pm/V. KTP is also transmissive only to about 4 μm [28]. When phase matching 1300 nm signal, this would problematically absorb the idler. However, when used in conjunction with PPLN, the PPKTP crystal would only need to operate at higher wavelength signals where the corresponding idler would transmit. Most importantly, KTP avoids higher order QPM of SHG at these signal wavelengths.

The main worry about KTP is its tendency to exhibit photochromic damage when pumped with high power IR lasers [76]. Also known as grey tracking, this effect causes the transmission to decrease over time, which could result in heating/damage and reduced signal power. It is sometimes reversible, but these variations in power are not ideal in the context of a controlled experiment.

5.1.3 Reducing RIN

Finally, the RIN of the seed signal discussed in Section 3.3.5 is not ideal for applications without the long integration times and high shot noise limits of TR-ARPES. There are several steps to take, the first of which is a careful analysis of the RF performance of the modulator (or a new one altogether). The RF port is optimized for multi-GHz telecom operation, not for tens of MHz. Accordingly, the RF port has been observed responding to DC voltages and causing substantial RF ringing (which is clearly visible in the contrast data, see Fig. 4.11). If we continue with this modulator, it must be properly terminated and AC coupled with an external circuit.

The other issue is the voltage sources. The pulse generator itself is the primary source of the 60 Hz noise, and a new, quieter device would certainly reflect in the laser RIN. The DC is currently much less of a problem, but an improved pulser noise figure would mean that a quieter DC source is also beneficial.

5.2 Future Impact

5.2.1 Applications of Broadband, Arbitrary Repetition Rate Fiber Lasers

The broadband, arbitrary repetition rate laser described in this thesis is a valuable tool for TR-ARPES, but other applications could also benefit from such a system. Other forms of pump-probe spectroscopy are a natural fit, with those requiring differential pump on/pump off measurements such as two-dimensional infrared spectroscopy (2D-IR) standing to benefit tremendously from arbitrary repetition rates [77]. The otherwise inflexible duty cycle of the nonlinear EDFA has motivated time-domain modulation of the pump/probe

delay rather than typical amplitude modulation, but this still limits the time scale of interest to the pulse-to-pulse period [78]. Using the scheme described in this thesis as an amplitude modulator, one could enable the study of relaxations on any time scale.

Precision femtosecond laser machining is also currently being optimized to incorporate duty cycle modulation in the MHz and GHz regime [79]. The highly programmable duty cycle of our system could allow unprecedented control over the machining process. Consecutive frequency conversion to the ultraviolet could also find use in surgery and low-resolution photolithography.

Frequency combs with repetition rates of 10-1000 GHz have seen substantial development in recent years. By using microresonators, CW lasers can form compact, broadband frequency combs [80, 81]. Additionally, HNLF schemes seeded with electro-optic combs are able to produce broad, flat-topped comb spectra in the telecom C-band (1525–1565 nm) [82]. The ability to vary the repetition rate of the comb could provide a unique source of broadband wavelength division multiplexing, as adjusting the repetition rate would change the wavelength channel spacing and could allow selective signal routing.

Nonlinear EDFA+HNLF schemes have already proven their ability to seed a broad range of amplifiers, including Ho/Tm [58–60], Yb, and OPAs [61]. The ability to seed these amplifiers on demand could unlock unprecedented, granular control of not only the repetition rate, but the pulse energy.

Appendix A

Additional Data

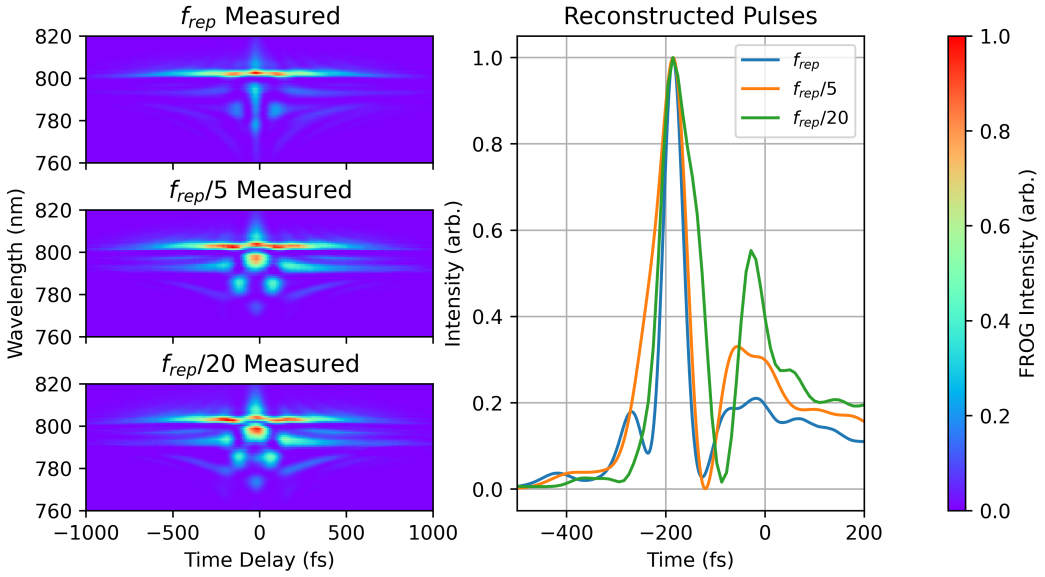

Figure A.1: Pulse reconstructions of SHG-FROG traces taken with optimized fiber lengths along the PM 1550 fast axis. Unlike the slow axis, the pulse shape is strongly dependent on the repetition rate, with neither the FROG traces nor their reconstructed pulses resembling one another. Interestingly, the pulse and FROG trace at f_{rep} do strongly resemble the slow axis measurement.

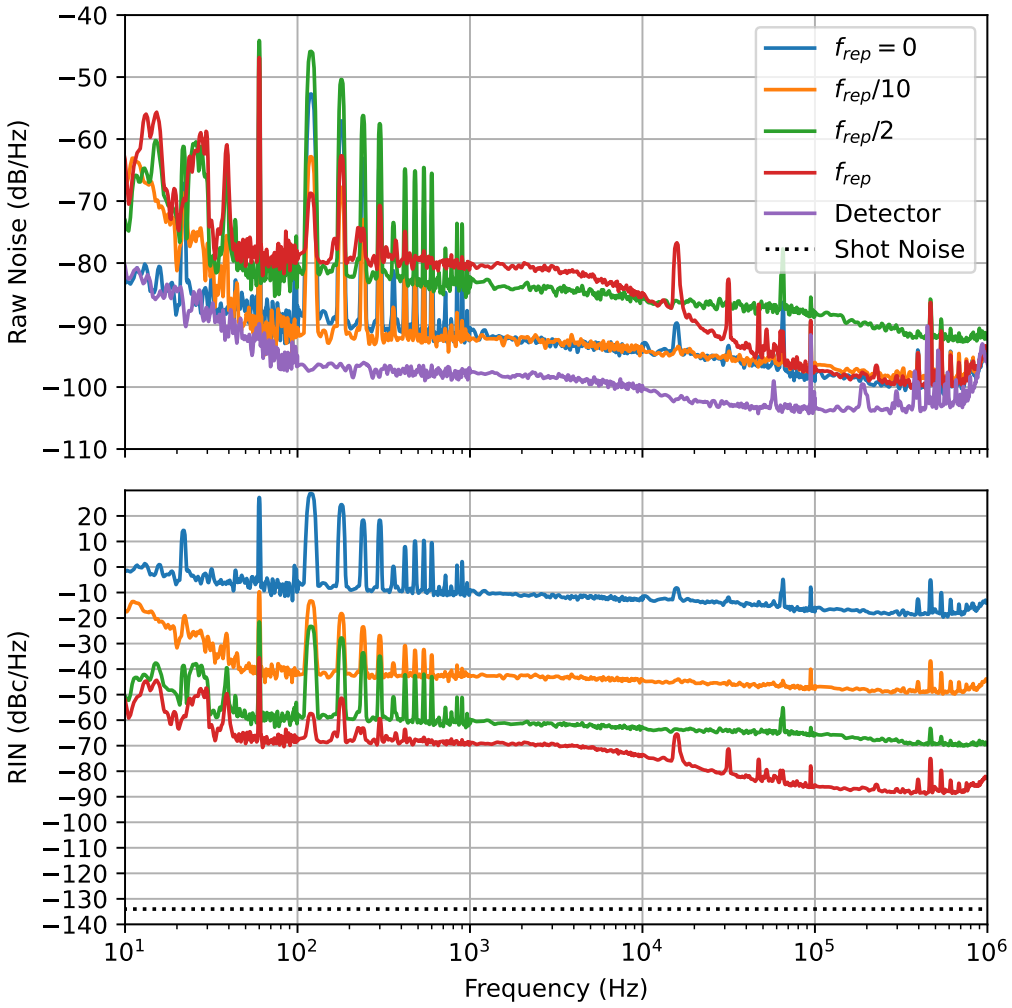

Figure A.2: Raw detector data and RIN spectra for the fast axis of the fiber after the polarization combiner. Note that in this case, f_{rep} receives no RF pulses, and the 60 Hz noise is much lower than other repetition rates.

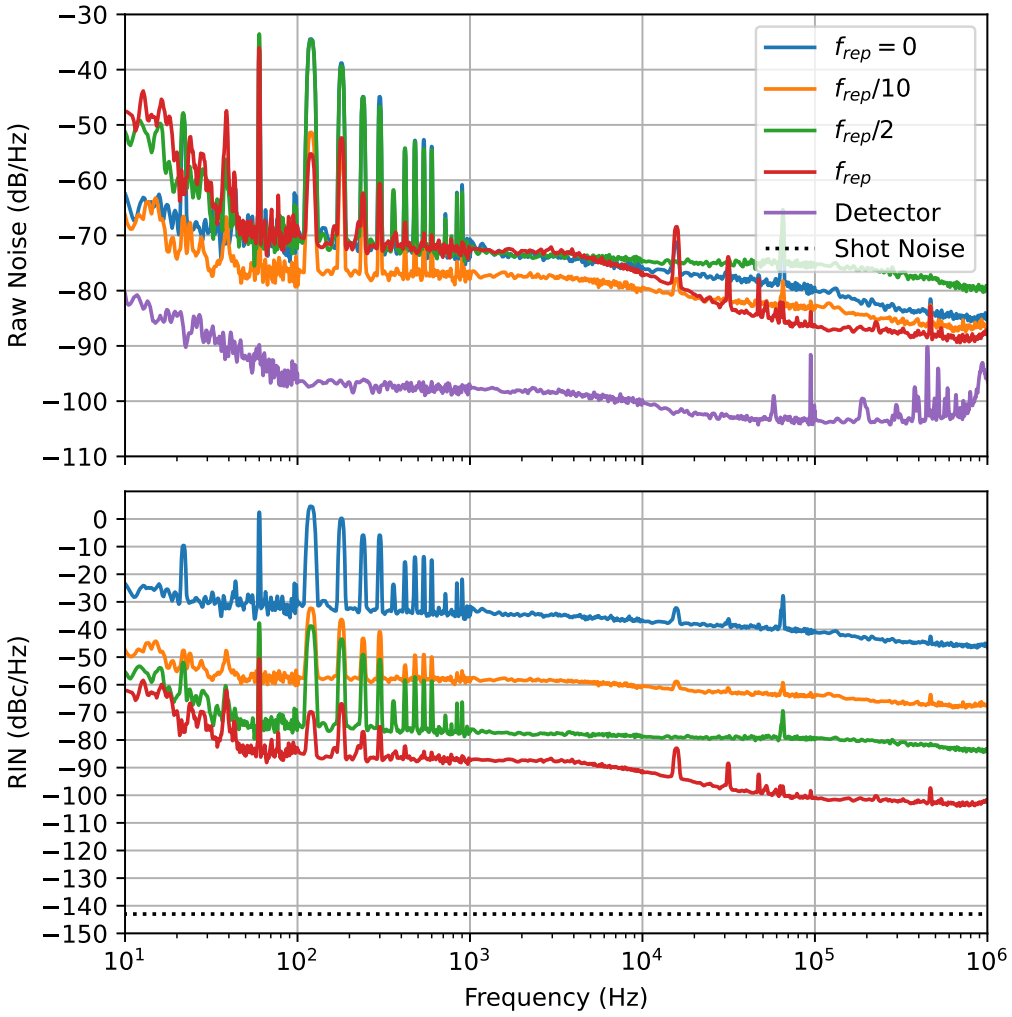

Figure A.3: Raw detector data and RIN spectra for the fast axis of the compression fiber. Note that in this case, f_{rep} receives no RF pulses, and the 60 Hz noise is much lower than other repetition rates.

Appendix B

Electronics

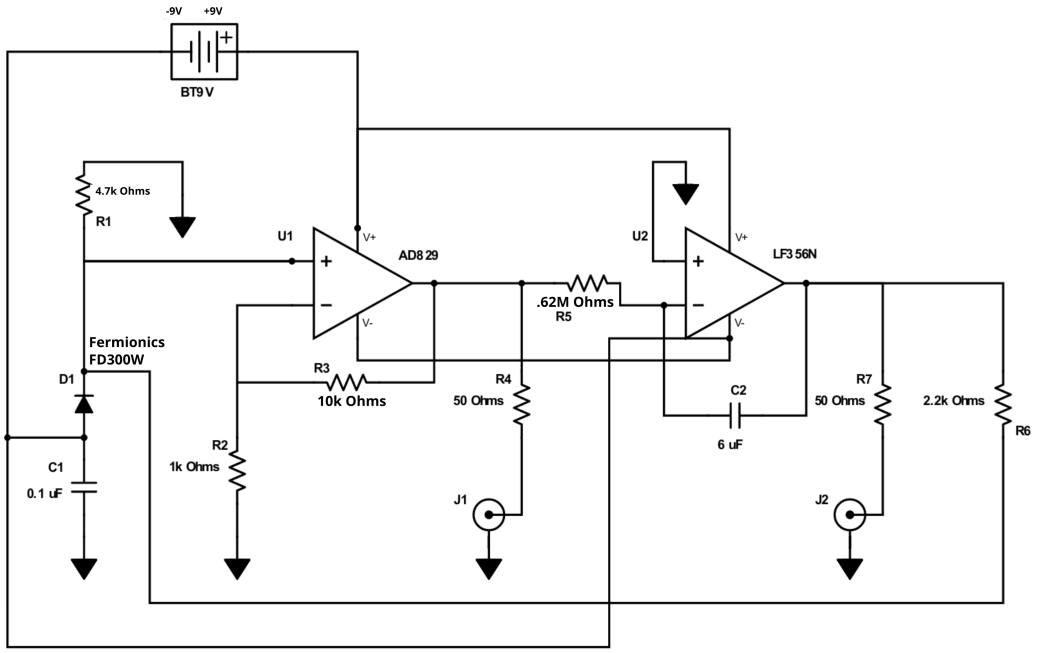

Figure B.1: Component diagram of the RIN detector used in Section 3.3.5.

Bibliography

[1] Stephan Hüfner. *Photoelectron Spectroscopy: Principles and Applications*. Springer Science & Business Media, March 2013. Google-Books-ID: f6nvCAAAQBAJ.

[2] T. A. Carlson. Photoelectron Spectroscopy. *Annual Review of Physical Chemistry*, 26(Volume 26,):211–234, October 1975. Publisher: Annual Reviews.

[3] K. Medjanik, O. Fedchenko, S. Chernov, D. Kutnyakhov, M. Ellguth, A. Oelsner, B. Schönhense, T. R. F. Peixoto, P. Lutz, C.-H. Min, F. Reinert, S. Däster, Y. Acremann, J. Viefhaus, W. Wurth, H. J. Elmers, and G. Schönhense. Direct 3D mapping of the Fermi surface and Fermi velocity. *Nature Materials*, 16(6):615–621, June 2017.

[4] B. Krömker, M. Escher, D. Funnemann, D. Hartung, H. Engelhard, and J. Kirschner. Development of a momentum microscope for time resolved band structure imaging. *Review of Scientific Instruments*, 79(5):053702, May 2008.

[5] S.V. Chernov, K. Medjanik, C. Tusche, D. Kutnyakhov, S.A. Nepijko, A. Oelsner, J. Braun, J. Minár, S. Borek, H. Ebert, H.J. Elmers, J. Kirschner, and G. Schönhense. Anomalous d-like surface resonances on Mo(110) analyzed by time-of-flight momentum microscopy. *Ultramicroscopy*, 159:453–463, December 2015.

[6] Jin Bakalis, Sergii Chernov, Ziling Li, Alice Kunin, Zachary H. Withers, Shuyu Cheng, Alexander Adler, Peng Zhao, Christopher Corder, Michael G. White, Gerd Schönhense, Xu Du, Roland Kawkami, and Thomas K. Allison. Momentum-space Observation of Optically Excited Non-Thermal Electrons in Graphene with Persistent Pseudospin Polarization, February 2024. arXiv:2402.13205 [cond-mat, physics:physics].

[7] Emma C. Regan, Danqing Wang, Eunice Y. Paik, Yongxin Zeng, Long Zhang, Jihang Zhu, Allan H. MacDonald, Hui Deng, and Feng Wang. Emerging exciton physics in transition metal dichalcogenide heterobilayers. *Nature Reviews Materials*, 7(10):778–795, May 2022.

[8] David Schmitt, Jan Philipp Bange, Wiebke Bennecke, AbdulAziz AlMutairi, Giuseppe Meneghini, Kenji Watanabe, Takashi Taniguchi, Daniel Steil, D. Russell Luke, R. Thomas Weitz, Sabine Steil, G. S. Matthijs Jansen, Samuel Brem, Ermin Malic, Stephan Hofmann, Marcel Reutzel, and Stefan Mathias. Formation of moiré interlayer excitons in space and time. *Nature*, 608(7923):499–503, August 2022.

[9] Ouri Karni, Elyse Barré, Vivek Pareek, Johnathan D. Georgaras, Michael K. L. Man, Chakradhar Sahoo, David R. Bacon, Xing Zhu, Henrique B. Ribeiro, Aidan L. O'Beirne, Jenny Hu, Abdullah Al-Mahboob, Mohamed M. M. Abdelrasoul, Nicholas S. Chan, Arka Karmakar, Andrew J. Winchester, Bumho Kim, Kenji Watanabe, Takashi Taniguchi, Katayun Barmak, Julien Madéo, Felipe H. da Jornada, Tony F. Heinz, and Keshav M. Dani. Structure of the moiré exciton captured by imaging its electron and hole. *Nature*, 603(7900):247–252, March 2022. Publisher: Nature Publishing Group.

[10] Alice Kunin, Sergey Chernov, Jin Bakalis, Ziling Li, Shuyu Cheng, Zachary H. Withers, Michael G. White, Gerd Schönhense, Xu Du, Roland K. Kawakami, and Thomas K. Allison. Momentum-Resolved Exciton Coupling and Valley Polarization Dynamics in Monolayer WS2. *Physical Review Letters*, 130(4):046202, January 2023. Publisher: American Physical Society.

[11] Gang Wang, Alexey Chernikov, Mikhail M. Glazov, Tony F. Heinz, Xavier Marie, Thierry Amand, and Bernhard Urbaszek. *Colloquium* : Excitons in atomically thin transition metal dichalcogenides. *Reviews of Modern Physics*, 90(2):021001, April 2018.

[12] Jan Philipp Bange, David Schmitt, Wiebke Bennecke, Giuseppe Meneghini, AbdulAziz AlMutairi, Kenji Watanabe, Takashi Taniguchi, Daniel Steil, Sabine Steil, R. Thomas Weitz, G. S. Matthijs Jansen, Stephan Hofmann, Samuel Brem, Ermin Malic, Marcel Reutzel, and Stefan Mathias. Probing electron-hole Coulomb correlations in the exciton landscape of a twisted semiconductor heterostructure. *Science Advances*, 10(6):eadi1323, February 2024. Publisher: American Association for the Advancement of Science.

[13] Thomas K. Allison, Zachary H. Withers, Ziling Li, Jin Bakalis, Sergii Chernov, Shuyu Cheng, Gerd Schönhense, Xu Du, Roland K. Kawakami, and Alice Kunin. Ultrafast dynamics in 2D materials and heterostructures visualized with time- and angle-resolved photoemission. In Markus Betz and Abdulhakem Y. Elezzabi, editors, *Ultrafast Phenomena and Nanophotonics XXVIII*, page 23, San Francisco, United States, March 2024. SPIE.

[14] J. Graf, S. Hellmann, C. Jozwiak, C. L. Smallwood, Z. Hussain, R. A. Kaindl, L. Kipp, K. Rossnagel, and A. Lanzara. Vacuum space charge effect in laser-based solid-state photoemission spectroscopy. *Journal of Applied Physics*, 107(1):014912, January 2010.

[15] Long Yuan, Biyuan Zheng, Jens Kunstmann, Thomas Brumme, Agnieszka Beata Kuc, Chao Ma, Shibin Deng, Daria Blach, Anlian Pan, and Libai Huang. Twist-angle-dependent interlayer exciton diffusion in WS2–WSe2 heterobilayers. *Nature Materials*, 19(6):617–623, June 2020.

[16] Stephanie Bettis Homan, Vinod K. Sangwan, Itamar Balla, Hadallia Bergeron, Emily A. Weiss, and Mark C. Hersam. Ultrafast Exciton Dissociation and Long-Lived Charge Separation in a Photovoltaic Pentacene–MoS2 van der Waals Heterojunction. *Nano Letters*, 17(1):164–169, January 2017. Publisher: American Chemical Society.

[17] M Ferray, A L'Huillier, X F Li, L A Lompre, G Mainfray, and C Manus. Multiple-harmonic conversion of 1064 nm radiation in rare gases. *Journal of Physics B: Atomic, Molecular and Optical Physics*, 21(3):L31–L35, February 1988.

[18] K. J. Schafer, Baorui Yang, L. F. DiMauro, and K. C. Kulander. Above threshold ionization beyond the high harmonic cutoff. *Physical Review Letters*, 70(11):1599–1602, March 1993.

[19] Lauryna Petraviciute Lötscher, Waldemar Schneider, Peter Rußbüldt, Bastian Gronloh, Hans-Dieter Hoffmann, Matthias F. Kling, and Alexander Apolonski. Direct low-harmonic generation in gas at MHz repetition rate. In *2013 Conference on Lasers & Electro-Optics Europe & International Quantum Electronics Conference CLEO EUROPE/IQEC*, pages 1–1, May 2013.

[20] T. K. Allison, A. Cingöz, D. C. Yost, and J. Ye. Extreme Nonlinear Optics in a Femtosecond Enhancement Cavity. *Physical Review Letters*, 107(18):183903, October 2011.

[21] Xinlong Li, Melanie A. R. Reber, Christopher Corder, Yuning Chen, Peng Zhao, and Thomas K. Allison. High-power ultrafast Yb:fiber laser frequency combs using commercially available components and basic fiber tools. *Review of Scientific Instruments*, 87(9):093114, September 2016.

[22] S. Mathias, L. Miaja-Avila, M. M. Murnane, H. Kapteyn, M. Aeschlimann, and M. Bauer. Angle-resolved photoemission spectroscopy with a femtosecond high harmonic light source using a two-dimensional imaging electron analyzer. *Review of Scientific Instruments*, 78(8):083105, August 2007.

[23] Peng Zhao, Xinlong Li, Matthew D. Kershis, Michael G. White, Thomas K. Allison, and Christopher Corder. Development of a tunable high repetition rate XUV source for time-resolved photoemission studies of ultrafast dynamics at surfaces. In Beat Neuenschwander, Gediminas Račiukaitis, Tetsuya Makimura, and Costas P. Grigoropoulos, editors, *Laser Applications in Microelectronic and Optoelectronic Manufacturing (LAMOM) XXIII*, page 10, San Francisco, United States, February 2018. SPIE.

[24] Robert W. Boyd. *Nonlinear optics*. Academic Press is an imprint of Elsevier, San Diego, 4 edition, 2019.

[25] Govind P. Agrawal. *Nonlinear fiber optics*. Optics and photonics. Academic Press, San Diego, 3. ed., [nachdr.] edition, 2005.

[26] C Manzoni and G Cerullo. Design criteria for ultrafast optical parametric amplifiers. *Journal of Optics*, 18(10):103501, October 2016.

[27] Anthony Catanese, Jay Rutledge, Myles C. Silfies, Xinlong Li, Henry Timmers, Abijith S. Kowligy, Alex Lind, Scott A. Diddams, and Thomas K. Allison. Mid-infrared frequency comb with 6.7 W average power based on difference frequency generation. *Optics Letters*, 45(5):1248, March 2020.

[28] Arlee V. Smith. *Crystal nonlinear optics: with SNLO examples*. AS-Photonics, Albuquerque, NM, 2nd edition edition, 2018.

[29] D. M. Krol, M. M. Broer, K. T. Nelson, R. H. Stolen, H. W. K. Tom, and W. Pleibel. Seeded second-harmonic generation in optical fibers: the effect of phase fluctuations. *Optics Letters*, 16(4):211–213, February 1991. Publisher: Optica Publishing Group.

[30] Dana Z. Anderson. Efficient Second-Harmonic Generation In Glass Fibers: The Possible Role Of Photo-Induced Charge Redistributiont. In *Nonlinear Optical Properties of Materials*, volume 1148, pages 186–196. SPIE, January 1990.

[31] M. Desaix, D. Anderson, and M. Lisak. Solitons emerging from pulses launched in the vicinity of the zero-dispersion point in a single-mode optical fiber. *Optics Letters*, 15(1):18, January 1990.

[32] Johan Hult. A Fourth-Order Runge–Kutta in the Interaction Picture Method for Simulating Supercontinuum Generation in Optical Fibers. *Journal of Lightwave Technology*, 25(12):3770–3775, December 2007.

[33] Gabriel Ycas. PyNLO, 2015.

[34] H.A. Haus. Mode-locking of lasers. *IEEE Journal of Selected Topics in Quantum Electronics*, 6(6):1173–1185, November 2000.

[35] D. E. Spence, P. N. Kean, and W. Sibbett. 60-fsec pulse generation from a self-mode-locked Ti:sapphire laser. *Optics Letters*, 16(1):42, January 1991.

[36] C. J. Saraceno, O. H. Heckl, C. R. E. Baer, C. Schriber, M. Golling, K. Beil, C. Kränkel, T. Südmeyer, G. Huber, and U. Keller. Sub-100 femtosecond pulses from a SESAM modelocked thin disk laser. *Applied Physics B*, 106(3):559–562, March 2012.

[37] Rüdiger Paschotta. *Field guide to lasers*. Number v. FG12 in SPIE field guides. SPIE Press, Bellingham, Wash, 2008.

[38] U. Morgner, F. X. Kärtner, S. H. Cho, Y. Chen, H. A. Haus, J. G. Fujimoto, E. P. Ippen, V. Scheuer, G. Angelow, and T. Tschudi. Sub-two-cycle pulses from a Kerr-lens mode-locked Ti:sapphire laser. *Optics Letters*, 24(6):411–413, March 1999. Publisher: Optica Publishing Group.

[39] Albrecht Bartels, Dirk Heinecke, and Scott A. Diddams. 10-GHz Self-Referenced Optical Frequency Comb. *Science*, 326(5953):681–681, October 2009. Publisher: American Association for the Advancement of Science.

[40] Kaoru Minoshima and Hirokazu Matsumoto. High-accuracy measurement of 240-m distance in an optical tunnel by use of a compact femtosecond laser. *Applied Optics*, 39(30):5512–5517, October 2000. Publisher: Optica Publishing Group.

[41] Paolo Ghelfi, Francesco Laghezza, Filippo Scotti, Giovanni Serafino, Amerigo Capria, Sergio Pinna, Daniel Onori, Claudio Porzi, Mirco Scaffardi, Antonio Malacarne, Valeria Vercesi, Emma Lazzeri, Fabrizio Berizzi, and Antonella Bogoni. A fully photonics-based coherent radar system. *Nature*, 507(7492):341–345, March 2014. Publisher: Nature Publishing Group.

[42] Katherine C. Phillips, Hemi H. Gandhi, Eric Mazur, and S. K. Sundaram. Ultrafast laser processing of materials: a review. *Advances in Optics and Photonics*, 7(4):684–712, December 2015. Publisher: Optica Publishing Group.

[43] Ahmed H. Zewail. Femtochemistry: Atomic-Scale Dynamics of the Chemical Bond. *The Journal of Physical Chemistry A*, 104(24):5660–5694, June 2000.

[44] Fritjof Helmchen and Winfried Denk. Deep tissue two-photon microscopy. *Nature Methods*, 2(12):932–940, December 2005. Publisher: Nature Publishing Group.

[45] Theodor W. Hänsch. Nobel Lecture: Passion for precision. *Reviews of Modern Physics*, 78(4):1297–1309, November 2006.

[46] John L. Hall. Nobel Lecture: Defining and measuring optical frequencies. *Reviews of Modern Physics*, 78(4):1279–1295, November 2006. Publisher: American Physical Society.

[47] Jungwon Kim and Youjian Song. Ultralow-noise mode-locked fiber lasers and frequency combs: principles, status, and applications. *Advances in Optics and Photonics*, 8(3):465, September 2016.

[48] Mark A. Foster, Amy C. Turner, Michal Lipson, and Alexander L. Gaeta. Nonlinear optics in photonic nanowires. *Optics Express*, 16(2):1300, 2008.

[49] Florian Tauser, Florian Adler, and Alfred Leitenstorfer. Widely tunable sub-30-fs pulses from a compact erbium-doped fiber source. *Optics Letters*, 29(5):516, March 2004.

[50] Alexander Sell, Günther Krauss, Rüdiger Scheu, Rupert Huber, and Alfred Leitenstorfer. 8-fs pulses from a compact Er:fiber system: quantitative modeling and experimental implementation. *Optics Express*, 17(2):1070, January 2009.

[51] Myles C. Silfies, Grzegorz Kowzan, Neomi Lewis, and Thomas K. Allison. Broadband cavity-enhanced ultrafast spectroscopy. *Physical Chemistry Chemical Physics*, 23(16):9743–9752, 2021.

[52] Hannes Kempf, Andrey Muraviev, Felix Breuning, Peter G. Schunemann, Ron Tenne, Alfred Leitenstorfer, and Konstantin Vodopyanov. Direct sampling of femtosecond electric-field waveforms from an optical parametric oscillator. *APL Photonics*, 9(3):036111, March 2024.

[53] Henry Timmers, Abijith Kowligy, Alex Lind, Flavio C. Cruz, Nima Nader, Myles Silfies, Gabriel Ycas, Thomas K. Allison, Peter G. Schunemann, Scott B. Papp, and Scott A. Diddams. Molecular fingerprinting with bright, broadband infrared frequency combs. *Optica*, 5(6):727, June 2018.

[54] Florian Tauser, Alfred Leitenstorfer, and Wolfgang Zinth. Amplified femtosecond pulses from an Er:fiber system: Nonlinear pulse shortening and selfreferencing detection of the carrier-envelope phase evolution. *Optics Express*, 11(6):594, March 2003.

[55] G. P. Agrawal. *Applications of nonlinear fiber optics*. Optics and photonics. Academic Press, San Diego, 2001.

[56] Daniele Brida, Günther Krauss, Alexander Sell, and Alfred Leitenstorfer. Ultrabroadband Er:fiber lasers. *Laser and Photonics Reviews*, 8(3):409–428, 2014.

[57] Günther Krauss, Sebastian Lohss, Tobias Hanke, Alexander Sell, Stefan Eggert, Rupert Huber, and Alfred Leitenstorfer. Synthesis of a single cycle of light with compact erbium-doped fibre technology. *Nature Photonics*, 4(1):33–36, January 2010.

[58] W. Hettel, G. Golba, D. Morrill, D. Carlson, P. Chang, T.-H. Wu, S. Diddams, H. Kapteyn, M. Murnane, and M. Hemmer. Compact, ultrastable, high repetition-rate 2 um and 3 um fiber laser for seeding mid-IR OPCPA. *Optics Express*, 32(3):4072, January 2024.

[59] C. Gaida, T. Heuermann, M. Gebhardt, E. Shestaev, T. P. Butler, D. Gerz, N. Lilienfein, P. Sulzer, M. Fischer, R. Holzwarth, A. Leitenstorfer, I. Pupeza, and J. Limpert. High-power frequency comb at 2 um wavelength emitted by a Tm-doped fiber laser system. *Optics Letters*, 43(21):5178, November 2018.

[60] Sida Xing, Abijith S. Kowligy, Daniel M. B. Lesko, Alexander J. Lind, and Scott A. Diddams. All-fiber frequency comb at 2 um providing 1.4-cycle pulses. *Optics Letters*, 45(9):2660, May 2020.

[61] Daniel L. Maser, Gabriel Ycas, William I. Depetri, Flavio C. Cruz, and Scott A. Diddams. Coherent frequency combs for spectroscopy across the 3–5 um region. *Applied Physics B*, 123(5):142, April 2017.

[62] Lars Grüner-Nielsen and Bera Pálsdóttir. Highly nonlinear fibers for very wideband supercontinuum generation. page 68731B, San Jose, CA, February 2008.

[63] J. Arnaud. Classical theory of laser noise. *Optical and Quantum Electronics*, 27(2):63–89, February 1995.

[64] V. Shumakova and O. H. Heckl. A short guide to recent developments in laser-based gas phase spectroscopy, applications, and tools. *APL Photonics*, 9(1):010803, January 2024.

[65] Myles C. Silfies, Grzegorz Kowzan, Yuning Chen, Neomi Lewis, Ryan Hou, Robin Baehre, Tobias Gross, and Thomas K. Allison. Widely tunable cavity-enhanced frequency combs. *Optics Letters*, 45(7):2123, April 2020.

[66] Rick P. Trebino. *Frequency-resolved optical gating: the measurement of ultrashort laser pulses*. Kluwer Academic Publishers, Boston Dordrecht London, 2002.

[67] Ieva Pipinytė, Viktorija Tamulienė, Julius Vengelis, Mantas Sirutavičius, Rimantas Grigonis, and Valdas Sirutkaitis. Investigation of laser-induced damage and related multiphoton absorption changes in lithium niobate crystals at high repetition rate femtosecond pump. *Optical Engineering*, 59(01):1, January 2020.

[68] E. N. Glezer, M. Milosavljevic, L. Huang, R. J. Finlay, T.-H. Her, J. P. Callan, and E. Mazur. Three-dimensional optical storage inside transparent materials. *Optics Letters*, 21(24):2023–2025, December 1996. Publisher: Optica Publishing Group.

[69] Vincent Pecheur, Henri Porte, Jérôme Hauden, Florent Bassignot, Moise Deroh, and Mathieu Chauvet. Watt-level SHG in undoped high step-index PPLN ridge waveguides. *OSA Continuum*, 4(5):1404–1414, May 2021. Publisher: Optica Publishing Group.

[70] Y. Furukawa, K. Kitamura, A. Alexandrovski, R. K. Route, M. M. Fejer, and G. Foulon. Green-induced infrared absorption in MgO doped LiNbO3. *Applied Physics Letters*, 78(14):1970–1972, April 2001.

[71] Jian Sun and Chang-qing Xu. Green-induced infrared absorption in annealed proton-exchanged MgO:LiNbO_3 waveguides. *Journal of the Optical Society of America B*, 31(11):2779, November 2014.

[72] A. R. Zanatta. The optical bandgap of lithium niobate (LiNbO3) and its dependence with temperature. *Results in Physics*, 39:105736, August 2022.

[73] Yuning Chen, Myles C. Silfies, Grzegorz Kowzan, Jose Miguel Bautista, and Thomas K. Allison. Tunable visible frequency combs from a Yb-fiber-laser-pumped optical parametric oscillator. *Applied Physics B*, 125(5):81, April 2019.

[74] MengXing Na, Arthur K. Mills, and David J. Jones. Advancing time- and angle-resolved photoemission spectroscopy: The role of ultrafast laser development. *Physics Reports*, 1036:1–47, October 2023.

[75] K. Moutzouris, F. Adler, F. Sotier, D. Träutlein, and A. Leitenstorfer. Multimilliwatt ultrashort pulses continuously tunable in the visible from a compact fiber source. *Optics Letters*, 31(8):1148, April 2006.

[76] B. Boulanger, I. Rousseau, J.P. Feve, M. Maglione, B. Menaert, and G. Marnier. Optical studies of laser-induced gray-tracking in KTP. *IEEE Journal of Quantum Electronics*, 35(3):281–286, March 1999. Conference Name: IEEE Journal of Quantum Electronics.

[77] Christopher T. Kuhs, Bradley M. Luther, and Amber T. Krummel. Recent Advances in 2D IR Spectroscopy Driven by Advances in Ultrafast Technology. *IEEE Journal of Selected Topics in Quantum Electronics*, 25(4):1–13, July 2019.

[78] C. Traum, P. Henzler, S. Lohner, H. Becker, D. Nabben, P. Gumbsheimer, C. Hinz, J. F. Lippmann, S. Mahapatra, K. Brunner, D. V. Seletskiy, and A. Leitenstorfer. Multicolor femtosecond pump-probe system

with single-electron sensitivity at low temperatures and high magnetic fields. *Review of Scientific Instruments*, 90(12):123003, 2019. _eprint: https://doi.org/10.1063/1.5126157.

[79] Andrius Žemaitis, Mantas Gaidys, Paulius Gečys, Martynas Barkauskas, and Mindaugas Gedvilas. Femtosecond laser ablation by bibursts in the MHz and GHz pulse repetition rates. *Optics Express*, 29(5):7641, March 2021.

[80] P. Del'Haye, A. Schliesser, O. Arcizet, T. Wilken, R. Holzwarth, and T. J. Kippenberg. Optical frequency comb generation from a monolithic microresonator. *Nature*, 450(7173):1214–1217, December 2007. Publisher: Nature Publishing Group.

[81] T. J. Kippenberg, R. Holzwarth, and S. A. Diddams. Microresonator-Based Optical Frequency Combs. *Science*, 332(6029):555–559, April 2011. Publisher: American Association for the Advancement of Science.

[82] Rui Wu, Victor Torres-Company, Daniel E. Leaird, and Andrew M. Weiner. Supercontinuum-based 10-GHz flat-topped optical frequency comb generation. *Optics Express*, 21(5):6045, March 2013.